J. Fluid Mech. (2011), *vol.* 667, *pp.* 474–519.
doi:10.1017/S0022112010004477

Shallow-water sloshing in vessels undergoing prescribed rigid-body motion in three dimensions

HAMID ALEMI ARDAKANI AND THOMAS J. BRIDGES†

Department of Mathematics, University of Surrey, Guildford, Surrey GU2 7XH, UK

(Received 17 December 2009; revised 20 August 2010; accepted 20 August 2010)

New shallow-water equations (SWEs), for sloshing in three dimensions (two horizontal and one vertical) in a vessel which is undergoing rigid-body motion in 3-space, are derived. The rigid-body motion of the vessel (roll–pitch–yaw and/or surge–sway–heave) is modelled exactly and the only approximations are in the fluid motion. The flow is assumed to be inviscid but vortical, with approximations on the vertical velocity and acceleration at the surface. These equations improve previous shallow-water models. The model also extends to three dimensions the essence of the Penney–Price–Taylor theory for the highest standing wave. The surface SWEs are simulated using a split-step alternating direction implicit finite-difference scheme. Numerical experiments are reported, including comparisons with existing results in the literature, and simulations with vessels undergoing full 3-D rotations.

Key words: rotating flows, surface gravity waves

1. Introduction

Shallow-water equations (SWEs) for a 3-D inviscid but vortical fluid in a vessel undergoing an arbitrary prescribed rigid-body motion in three dimensions are derived. The rigid-body motion is represented exactly and only two assumptions are imposed on the velocity and acceleration at the free surface to close the SWEs.

While there has been a vast amount of research into 2-D sloshing, the research into 3-D sloshing is still very much in development. A review of much of the research to date is presented in Ibrahim (2005) and Faltinsen & Timokha (2009). The predominant theoretical approaches for studying 3-D sloshing are (*a*) asymptotics and weakly nonlinear theories, (*b*) multi-modal expansions which reduce the governing equations to a set of ordinary differential equations (ODEs); (*c*) reduction to model partial differential equations (PDEs) such as the SWEs; and (*d*) direct numerical simulation of the full 3-D problem.

If 3-D numerical simulations were faster, the latter approach would be very appealing. There has been much progress in the numerical simulation of 3-D sloshing using Navier–Stokes based methods (MAC, SOLA-SURF, VOF, RANSE), boundary-element methods and finite-element methods for 3-D potential flow (some examples are Wu, Ma & Eatock Taylor 1998; Cariou & Casella 1999; Chen, Hwang & Ko 2000; Gerrits 2001; Kim 2001; Buchner 2002; aus der Wiesche 2003; Kleefsman *et al.* 2005; Lee *et al.* 2007; Liu & Lin 2008; Chen, Djidjeli & Price 2009). Rebouillat & Liksonov (2010) review a range of numerical strategies for fully 3-D sloshing. While the results

† Email address for correspondence: t.bridges@surrey.ac.uk

of these simulations are impressive, the difficulty is that CPU times are measured in hours rather than minutes or seconds. An example is the VOF simulations of Liu & Lin (2008), where 3-D sloshing in a vessel with rectangular base is forced harmonically. To simulate 50 s of real time (about 20 periods of harmonic forcing) took 265 h of CPU time. It is very difficult to do parametric studies or long-time simulations with this amount of CPU time. Hence, any reduction in dimension is appealing.

On the other hand, one can make some progress in the understanding of sloshing in three dimensions using analytical methods, asymptotics (perturbation theory, multi-scale expansions) and modal expansions. In 2-D shallow-water sloshing, the predominant types of solution are the standing wave and travelling hydraulic jump. But in 3-D shallow-water sloshing, the range of basic solutions is much larger. One still has the 2-D solutions, but there can be mixed modes, swirling modes, multi-mode cnoidal standing waves, diagonal modes and multi-dimensional hydraulic jumps, and analytical methods are very effective for identifying parameter regimes for these basic solutions (e.g. Bridges 1987; Faltinsen & Timokha 2003; Faltinsen, Rognebakke & Timokha 2003, 2006*a*). Also, there is a vast literature on asymptotic methods for the special case of parametrically forced sloshing in rectangular containers (Faraday experiment) (e.g. Miles & Henderson 1990, and its citation trail). Multi-modal expansions take analytic methods to higher order. When the fluid domain is finite in extent, there is a countable basis of eigenfunctions for the basin shape, and one approach that has been extensively used is to expand the nonlinear equations in terms of these (or other) basis functions with time-dependent coefficients, leading to a large system of ODEs. Examples of this approach are Faltinsen & Timokha (2003), Faltinsen *et al.* (2003, 2006*a*), La Rocca, Mele & Armenio (1997), La Rocca, Sciortino & Boniforti (2000) and Part II of Ibrahim (2005). The advantage of modal approximation is that the problem is reduced to a system of ODEs which is much quicker to simulate numerically.

In between direct 3-D simulations and analytical methods is a third approach: to derive reduced PDE models. This approach is particularly useful for the study of shallow-water sloshing. The study of 3-D shallow-water sloshing is motivated by a number of applications such as sloshing on the deck of fishing vessels (Adee & Caglayan 1982; Caglayan & Storch 1982) and offshore supply vessels (Falzarano, Laranjinha & Guedes Soares 2002), sloshing in wing fuel tanks of aircraft (Disimile, Pyles & Toy 2009), green-water effects (Dillingham & Falzarano 1986; Zhou, Kat & Buchner 1999; Buchner 2002; Kleefsman *et al.* 2005), sloshing in a swimming pool on deck (Ruponen *et al.* 2009), sloshing in fish tanks onboard fishing vessels (Lee, Surendran & Lee 2005) and sloshing in automobile fuel tanks (aus der Wiesche 2003).

About the same time, Dillingham & Falzarano (1986) and Pantazopoulos (1987) (see also Pantazopoulos & Adee 1987 and Pantazopoulos 1988) derived SWEs for 3-D sloshing with the vessel motion prescribed. It is this approach that is the starting point for the current paper. These SWEs, hereafter called the DFP SWEs, will be recorded and analysed in § 10. In follow-up work, Huang (1995) (see also Huang & Hsiung 1996, 1997) gave an alternative derivation of rotating SWEs for sloshing, resulting in slightly different equations from the DFP SWEs. The latter system will be called the HH SWEs. A discussion of the HH SWEs is also given in § 10.

The DFP SWEs use a very simple form for the vessel motion, and have unnecessarily restrictive assumptions in the derivation. The derivation of the HH SWEs is more precise but still has some restrictive assumptions. These assumptions are outlined in § 10 and, in more detail, in the technical reports of Alemi Ardakani & Bridges (2009*c*, *d*).

In this paper, a new derivation of SWEs is given in three dimensions. The starting point for the new SWEs is the exact equation for the horizontal velocity field at the free surface

$$\left.\begin{aligned} U_t + UU_x + VU_y + \left(a_{11} + \frac{\mathrm{D}w}{\mathrm{D}t}\Big|^h\right) h_x + a_{12}h_y &= b_1 + \sigma\,\partial_x \mathrm{div}(\boldsymbol{\kappa}),\\ V_t + UV_x + VV_y + \left(a_{22} + \frac{\mathrm{D}w}{\mathrm{D}t}\Big|^h\right) h_y + a_{21}h_x &= b_2 + \sigma\,\partial_y \mathrm{div}(\boldsymbol{\kappa}). \end{aligned}\right\} \tag{1.1}$$

These equations are relative to a frame of reference moving with the vessel with coordinates (x, y, z) and z normal to the vessel base. The terms $a_{11}, a_{12}, a_{21}, a_{22}, b_1, b_2$ encode the moving frame, $\boldsymbol{\kappa}$ is minus the horizontal projection of the unit normal of the surface and is defined in § 2, σ is the coefficient of surface tension and $\mathrm{D}w/\mathrm{D}t|^h$ is the Lagrangian vertical acceleration evaluated at the free surface. The fluid occupies a rectangular region with a single-valued free surface,

$$0 \leqslant z \leqslant h(x, y, t), \quad 0 \leqslant x \leqslant L_1, \quad 0 \leqslant y \leqslant L_2. \tag{1.2}$$

The free-surface horizontal velocity field is

$$U(x, y, t) = u(x, y, z, t)|^h := u(x, y, h(x, y, t), t) \quad \text{and} \quad V(x, y, t) = v(x, y, z, t)|^h. \tag{1.3}$$

Couple (1.1) with the exact mass conservation equation,

$$h_t + (hU)_x + (hV)_x = W + hU_x + hV_y, \tag{1.4}$$

which is derived from the kinematic free-surface boundary condition (see § 2). $W = w|^h$ is the vertical velocity at the free surface.

By assuming that $\mathrm{D}w/\mathrm{D}t|^h \approx 0$ and $W + hU_x + hV_y \approx 0$, (1.1)–(1.4) are a closed set of SWEs which retain the vessel motion exactly. It is this closed set of SWEs that is the starting point for the analysis and numerics in this paper.

One of the advantages of the SWEs is that vorticity is retained. This is in contrast to almost all analytical research into 3-D sloshing which is based on the assumption of irrotationality. Vorticity can be input through the initial conditions, but a new mechanism comes into play in shallow-water sloshing: the creation of vorticity though discontinuities in hydraulic jumps (e.g. Pratt 1983; Peregrine 1998, 1999). In coastal hydraulics, Peregrine (1998) has shown how steady hydraulic jumps generate vorticity – *for a steady flow*. In the case of shallow-water sloshing, there is a new dynamic mechanism due to the time-dependent nature of the hydraulic jumps, and the new equations give some direction towards generalizing the Pratt–Peregrine theory to the unsteady case. The emergence of non-zero vertical vorticity is witnessed in some of the numerical simulations reported herein.

The surface equations (1.1)–(1.4) have a form of potential vorticity (PV) conservation, when (*a*) surface tension is neglected; (*b*) Lagrangian vertical accelerations are neglected; and (*c*) the vertical velocity is approximated by $W \approx -hU_x - hV_y$. In this case, the PV is

$$\mathrm{PV} = \frac{V_x - U_y + 2\Omega_3 - 2\Omega_2 h_y - 2\Omega_1 h_x}{h}. \tag{1.5}$$

In the special case where $\Omega_1 = \Omega_2 = 0$ and Ω_3 is constant, the expression for PV reduces to the classical case in geophysical fluid dynamics (e.g. § 4.2 of Salmon 1998). When Ω_1 and Ω_2 are non-zero, there is an interesting geometrical interpretation: the

correction to the vertical vorticity is the projection of the angular velocity vector onto the surface unit normal. See § 8 for details. In geophysical fluid dynamics, the rotation vector (rotation of the earth) is treated as a constant and is always vertical. On the other hand, Barnes *et al.* (1983) have shown that the earth does indeed wobble and so the idea of a time-dependent rotation vector as here may have some interest in geophysical fluid dynamics.

The vessel is modelled as a rigid body, and the position of a rigid body in 3-space is completely determined by specifying $(\boldsymbol{q}(t), \boldsymbol{Q}(t))$, where $\boldsymbol{q}(t)$ is a vector in $\mathbb{R}^3$, giving the horizontal and vertical translations of the body relative to some fixed reference frame, and $\boldsymbol{Q}$ is a proper 3×3 rotation matrix. ($\boldsymbol{Q}$ is orthogonal and $\det(\boldsymbol{Q}) = 1$.)

Specifying translations is straightforward, but specifying rotations requires a little more care. Surprisingly, most previous work on forced sloshing uses pure translation, or the rotations are simplified using a small-angle approximation or restricted to planar rotations. The small-angle approximation is to take the angular velocity of the form $\boldsymbol{\Omega} = (\dot{\phi}, \dot{\theta}, \dot{\psi})$, where ϕ, θ and ψ are roll, pitch and yaw angles, respectively (precise definition given in § C.1). Examples of forcing used in the literature are Chen *et al.* (2009) (harmonic surge and sway motion, and harmonic roll motion), Wu *et al.* (1998) (harmonic surge, sway and heave forcing), Chen *et al.* (2000) and Faltinsen *et al.* (2006*a*) (harmonic surge forcing), aus der Wiesche (2003) (impulse excitation representative of automobile accelerations), Faltinsen, Rognebakke & Timokha (2006*b*) (roll–pitch forcing with a small-angle approximation), Faltinsen *et al.* (2003) (roll–pitch–surge–sway forcing with small-angle approximation for rotations), Liu & Lin (2008) and Wu & Chen (2009) (forcing in all six degrees of freedom with small-angle approximation for rotations).

In this paper, exact coordinate-independent 3-D representations of the rotations are used. Special coordinate choices are Euler-angle representations and numerical construction of the rotation matrix. The choice (body or space) representation of the angular velocity is important and its implications are discussed. Also there are subtleties in the construction of the angular velocity (Leubner 1981), and these are also discussed herein and in the report of Alemi Ardakani & Bridges (2009*e*).

There has been very little experimental work with vessels undergoing full 3-D rotations. Most experiments are with pure translations and/or planar rotations. A facility for 3-D rotations of vessels with fluid would be technically demanding. However, the paper of Disimile *et al.* (2009) mentions an experimental facility capable of exciting a tank containing fluid in all six degrees of freedom. However, to date, they have reported only on results of forced roll motion.

Our principal tool for analysing the SWEs is numerics. The numerical scheme is based on the Abbott–Ionescu scheme which is widely used in computational hydraulics. It is a finite-difference scheme, fully implicit, and the two-dimensionality is treated using an alternating direction implicit scheme. A 1-D version of this scheme was used in Alemi Ardakani & Bridges (2009*a*).

An overview of the paper is as follows. In §§ 3 and 4, the surface equations (1.1) for sloshing in a vessel undergoing motion in 3-space are derived starting from the full 3-D Euler equations relative to a moving frame. Before assuming that the Lagrangian vertical accelerations are small, we analyse the exact equations in § 5 and show that they give an explanation for and a generalization to three dimensions of the Penney–Price–Taylor theory for the highest standing wave. The assumptions necessary for the reduction to a closed set of SWEs with the exact body motion are discussed in § 7, leading to a closed set of SWEs. PV conservation is discussed in § 8.

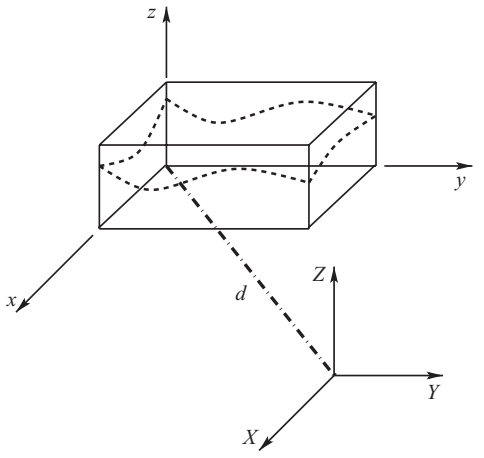

FIGURE 1. Schematic showing a configuration of the fixed coordinate system $OXYZ$ relative to the moving coordinate system, attached to the tank, $Oxyz$. The origin of the $OXYZ$ coordinate system can have an additional displacement $\boldsymbol{q}(t)$. In this figure, $\boldsymbol{q}(t)=0$.

Details of the specification of the vessel motion are given in § 9, including both an Euler-angle representation and direct calculation of the rotation matrix numerically. Further detail on the special case of yaw–pitch–roll Euler angles is given in the report of Alemi Ardakani & Bridges (2009*b*).

The DFP SWEs and HH SWEs are reviewed in the reports of Alemi Ardakani & Bridges (2009*c*) and Alemi Ardakani & Bridges (2009*d*). A summary of the main assumptions in their derivation and a comparison with the new surface SWEs is given in § 10.

Numerical results are reported in §§ 12–15. These simulations include full 3-D rotations: roll–pitch and roll–pitch–yaw in § 12. Results of pure yaw forcing are reported in § 13. These simulations show the appearance of vorticity and agree with previous simulations of Huang & Hsiung (1996). Motivated by the theory of Faltinsen *et al.* (2003) and the simulations of Wu & Chen (2009), diagonal surge–sway forcing is considered in § 14, capturing diagonal waves and swirling waves. In § 15, an example is shown with very large displacements of the vessel. The model is based on the London Eye, but its implications are much more general, as it illustrates how the model can be effectively applied to motion of the vehicle along arbitrarily defined surfaces.

2. Governing equations

The configuration of the fluid in a rotating–translating vessel is schematically shown in figure 1. The vessel is a rigid body, which is free to rotate and or translate in $\mathbb{R}^3$, and this motion will be specified. The spatial frame, which is fixed in space, has coordinates denoted by $\boldsymbol{X}=(X, Y, Z)$, and the body frame – a moving frame – is attached to the vessel and has coordinates denoted by $\boldsymbol{x}=(x, y, z)$.

The whole system is translating in space with translation vector $\boldsymbol{q}(t)$. The position of a particle in the body frame is therefore related to a point in the spatial frame by

$$\boldsymbol{X}=\boldsymbol{Q}(\boldsymbol{x}+\boldsymbol{d})+\boldsymbol{q}, \tag{2.1}$$

where $\boldsymbol{Q}$ is a proper rotation in $\mathbb{R}^3$ ($\boldsymbol{Q}^{\mathrm{T}}=\boldsymbol{Q}^{-1}$ and $\det(\boldsymbol{Q})=1$). The axis of rotation can be displaced by a distance $\boldsymbol{d}$ from the origin of the body frame and $\boldsymbol{d}=(d_1, d_2, d_3)\in\mathbb{R}^3$

is constant. The displacement $\boldsymbol{Qd}$ could be incorporated into $\boldsymbol{q}(t)$, but in cases where the origin of the spatial frame is fixed, it will be useful to maintain the distinction.

This formulation is consistent with the theory of rigid-body motion, where an arbitrary motion can be described by the pair $(\boldsymbol{Q}(t), \boldsymbol{q}(t))$, with $\boldsymbol{Q}(t)$ being a proper rotation matrix and $\boldsymbol{q}(t)$ a vector in $\mathbb{R}^3$ (Murray, Lin & Sastry 1994; O'Reilly 2008).

The *body angular velocity* is a time-dependent vector,

$$\boldsymbol{\Omega}(t) = (\Omega_1(t), \Omega_2(t), \Omega_3(t)), \tag{2.2}$$

with entries determined from $\boldsymbol{Q}$ by

$$\boldsymbol{Q}^{\mathrm{T}}\dot{\boldsymbol{Q}} = \begin{bmatrix} 0 & -\Omega_3 & \Omega_2 \\ \Omega_3 & 0 & -\Omega_1 \\ -\Omega_2 & \Omega_1 & 0 \end{bmatrix} := \widehat{\boldsymbol{\Omega}}. \tag{2.3}$$

The convention for the entries of the skew-symmetric matrix $\widehat{\Omega}$ is such that

$$\widehat{\boldsymbol{\Omega}}\boldsymbol{r} = \boldsymbol{\Omega} \times \boldsymbol{r}, \quad \text{for any} \quad \boldsymbol{r} \in \mathbb{R}^3, \quad \boldsymbol{\Omega} := (\Omega_1, \Omega_2, \Omega_3). \tag{2.4}$$

The body angular velocity is to be contrasted with the *spatial angular velocity* – the angular velocity viewed from the spatial frame – which is

$$\widehat{\boldsymbol{\Omega}}^{spatial} := \dot{\boldsymbol{Q}}\boldsymbol{Q}^{\mathrm{T}}. \tag{2.5}$$

As vectors, the spatial and body angular velocities are related by $\boldsymbol{\Omega}^{spatial} = \boldsymbol{Q}\boldsymbol{\Omega}$. Either representation can be used for the angular velocity. For example, Pantazopoulos (1988), Dillingham & Falzarano (1986), Falzarano *et al.* (2002) and Pantazopoulos & Adee (1987) use the spatial representation, whereas Huang & Hsiung (1996, 1997) use the body representation. We will show that the body representation is the sensible choice leading to great simplification of the equations. Henceforth, the angular velocity without a superannotation will represent the body angular velocity.

The velocity and acceleration in the spatial frame are

$$\dot{\boldsymbol{X}} = \boldsymbol{Q}(\dot{\boldsymbol{x}} + \boldsymbol{\Omega} \times (\boldsymbol{x} + \boldsymbol{d})) + \dot{\boldsymbol{q}}, \tag{2.6}$$

and

$$\ddot{\boldsymbol{X}} = \boldsymbol{Q}[\ddot{\boldsymbol{x}} + 2\boldsymbol{\Omega} \times \dot{\boldsymbol{x}} + \dot{\boldsymbol{\Omega}} \times (\boldsymbol{x} + \boldsymbol{d}) + \boldsymbol{\Omega} \times \boldsymbol{\Omega} \times (\boldsymbol{x} + \boldsymbol{d}) + \boldsymbol{Q}^{\mathrm{T}}\ddot{\boldsymbol{q}}]. \tag{2.7}$$

Newton's law is expressed relative to the spatial frame, but substitution of (2.6)–(2.7) into Newton's law and multiplying by $\boldsymbol{Q}^{\mathrm{T}}$ gives the governing equations relative to the body frame,

$$\frac{\mathrm{D}\boldsymbol{u}}{\mathrm{D}t} + \frac{1}{\rho}\nabla p + 2\boldsymbol{\Omega} \times \boldsymbol{u} + \dot{\boldsymbol{\Omega}} \times (\boldsymbol{x} + \boldsymbol{d}) + \boldsymbol{\Omega} \times (\boldsymbol{\Omega} \times (\boldsymbol{x} + \boldsymbol{d})) + \boldsymbol{Q}^{\mathrm{T}}\boldsymbol{g} + \boldsymbol{Q}^{\mathrm{T}}\ddot{\boldsymbol{q}} = 0, \tag{2.8}$$

where $\boldsymbol{u} = (u, v, w)$ is the velocity field,

$$\frac{\mathrm{D}}{\mathrm{D}t} := \frac{\partial}{\partial t} + u\frac{\partial}{\partial x} + v\frac{\partial}{\partial y} + w\frac{\partial}{\partial z} \quad \text{and} \quad \boldsymbol{g} := g\begin{pmatrix} 0 \\ 0 \\ 1 \end{pmatrix}, \tag{2.9}$$

with $g > 0$ being the gravitational constant. A detailed derivation is given in Appendix A of Alemi Ardakani & Bridges (2009*a*). The term $\boldsymbol{Q}^{\mathrm{T}}\boldsymbol{g}$ rotates the usual gravity vector so that its direction is viewed properly in the body frame. The same is true for the translational acceleration $\ddot{\boldsymbol{q}}$. Further comments on the viewpoint of the vessel velocity and acceleration are presented in § 9.

In the derivation of the SWEs, the components of (2.8) will be needed. We write the momentum equation as

$$\frac{\mathrm{D}\boldsymbol{u}}{\mathrm{D}t} + \frac{1}{\rho}\nabla p = \boldsymbol{F}. \tag{2.10}$$

Then

$$\boldsymbol{F} = -2\boldsymbol{\Omega}\times\boldsymbol{u} - \dot{\boldsymbol{\Omega}}\times(\boldsymbol{x}+\boldsymbol{d}) - \boldsymbol{\Omega}\times(\boldsymbol{\Omega}\times(\boldsymbol{x}+\boldsymbol{d})) - \boldsymbol{Q}^{\mathrm{T}}\boldsymbol{g} - \boldsymbol{Q}^{\mathrm{T}}\ddot{\boldsymbol{q}}, \tag{2.11}$$

and the components of $\boldsymbol{F}$ are

$$\left.\begin{aligned} F_1 &= -2(\Omega_2 w - \Omega_3 v) - \dot{\Omega}_2(z+d_3) + \dot{\Omega}_3(y+d_2) \\ &\quad -\Omega_1\,\boldsymbol{\Omega}\cdot(\boldsymbol{x}+\boldsymbol{d}) + (x+d_1)\|\boldsymbol{\Omega}\|^2 - \ddot{\boldsymbol{q}}\cdot\boldsymbol{Q}\boldsymbol{e}_1 - g\boldsymbol{e}_3\cdot\boldsymbol{Q}\boldsymbol{e}_1, \\ F_2 &= +2(\Omega_1 w - \Omega_3 u) + \dot{\Omega}_1(z+d_3) - \dot{\Omega}_3(x+d_1) \\ &\quad -\Omega_2\,\boldsymbol{\Omega}\cdot(\boldsymbol{x}+\boldsymbol{d}) + (y+d_2)\|\boldsymbol{\Omega}\|^2 - \ddot{\boldsymbol{q}}\cdot\boldsymbol{Q}\boldsymbol{e}_2 - g\boldsymbol{e}_3\cdot\boldsymbol{Q}\boldsymbol{e}_2, \\ F_3 &= -2(\Omega_1 v - \Omega_2 u) - \dot{\Omega}_1(y+d_2) + \dot{\Omega}_2(x+d_1) \\ &\quad -\Omega_3\,\boldsymbol{\Omega}\cdot(\boldsymbol{x}+\boldsymbol{d}) + (z+d_3)\|\boldsymbol{\Omega}\|^2 - \ddot{\boldsymbol{q}}\cdot\boldsymbol{Q}\boldsymbol{e}_3 - g\boldsymbol{e}_3\cdot\boldsymbol{Q}\boldsymbol{e}_3. \end{aligned}\right\} \tag{2.12}$$

The use of the unit vectors $\boldsymbol{e}_1$, $\boldsymbol{e}_2$ and $\boldsymbol{e}_3$ is just to compactify notation. The terms with unit vectors are interpreted as

$$\boldsymbol{Q}\boldsymbol{e}_3\cdot\boldsymbol{e}_3 = Q_{33}, \tag{2.13}$$

where Q_{ij} is the (i,j)th entry of the matrix representation of $\boldsymbol{Q}$ and

$$\boldsymbol{Q}\boldsymbol{e}_3\cdot\ddot{\boldsymbol{q}} = Q_{13}\ddot{q}_1 + Q_{23}\ddot{q}_2 + Q_{33}\ddot{q}_3, \tag{2.14}$$

with similar expressions for the other such terms.

The fluid occupies the region

$$0 \leqslant x \leqslant L_1, \quad 0 \leqslant y \leqslant L_2, \quad 0 \leqslant z \leqslant h(x,y,t), \tag{2.15}$$

where the lengths L_1 and L_2 are given positive constants, and $z = h(x,y,t)$ is the position of the free surface.

Conservation of mass relative to the body frame takes the usual form

$$u_x + v_y + w_z = 0. \tag{2.16}$$

The boundary conditions are

$$\left.\begin{aligned} u = 0 \quad &\text{at} \quad x = 0 \quad \text{and} \quad x = L_1, \\ v = 0 \quad &\text{at} \quad y = 0 \quad \text{and} \quad y = L_2, \\ &\qquad w = 0 \quad \text{at} \quad z = 0, \end{aligned}\right\} \tag{2.17}$$

and, at the free surface, the boundary conditions are the kinematic condition

$$h_t + uh_x + vh_y = w, \quad \text{at} \quad z = h(x,y,t), \tag{2.18}$$

and the dynamic condition

$$p = -\rho\sigma\,\mathrm{div}(\boldsymbol{\kappa}) \quad \text{at} \quad z = h(x,y,t), \tag{2.19}$$

where $\sigma > 0$ is the coefficient of surface tension,

$$\mathrm{div}(\boldsymbol{\kappa}) = \frac{\partial\kappa_1}{\partial x} + \frac{\partial\kappa_2}{\partial y}, \tag{2.20}$$

and

$$\kappa_1 = \frac{h_x}{\sqrt{1+h_x^2+h_y^2}} \quad \text{and} \quad \kappa_2 = \frac{h_y}{\sqrt{1+h_x^2+h_y^2}}. \tag{2.21}$$

The vector $\boldsymbol{\kappa}$ is minus the horizontal component of the unit normal at the free surface. The unit normal vector $\boldsymbol{n}$ to the free surface, chosen to point out of the fluid, is

$$\boldsymbol{n} = \frac{1}{\ell}\begin{pmatrix} -h_x \\ -h_y \\ 1 \end{pmatrix}, \quad \ell = \sqrt{1+h_x^2+h_y^2}. \tag{2.22}$$

2.1. *Vorticity*

The vorticity vector is defined by

$$\mathcal{V} := \nabla \times \boldsymbol{u}. \tag{2.23}$$

Differentiating this equation gives

$$\frac{\mathrm{D}\mathcal{V}}{\mathrm{D}t} = \mathcal{V}\cdot\nabla\boldsymbol{u} + \nabla \times \left(\frac{\mathrm{D}\boldsymbol{u}}{\mathrm{D}t}\right). \tag{2.24}$$

Taking the curl of the momentum equations (2.8) gives

$$\nabla \times \left(\frac{\mathrm{D}\boldsymbol{u}}{\mathrm{D}t}\right) = 2\boldsymbol{\Omega}\cdot\nabla\boldsymbol{u} - 2\dot{\boldsymbol{\Omega}}. \tag{2.25}$$

Combining with (2.24) gives the vorticity equation

$$\frac{\mathrm{D}\mathcal{V}}{\mathrm{D}t} = (2\boldsymbol{\Omega}+\mathcal{V})\cdot\nabla\boldsymbol{u} - 2\dot{\boldsymbol{\Omega}}. \tag{2.26}$$

Two components of the vorticity equation will be important in the derivation of the surface SWEs,

$$\left.\begin{aligned} \frac{\partial}{\partial y}\left(\frac{\mathrm{D}w}{\mathrm{D}t}\right) &= \frac{\partial}{\partial z}\left(\frac{\mathrm{D}v}{\mathrm{D}t}\right) + 2\Omega_1\frac{\partial u}{\partial x} + 2\Omega_2\frac{\partial u}{\partial y} + 2\Omega_3\frac{\partial u}{\partial z} - \dot{\Omega}_1, \\ \frac{\partial}{\partial x}\left(\frac{\mathrm{D}w}{\mathrm{D}t}\right) &= \frac{\partial}{\partial z}\left(\frac{\mathrm{D}u}{\mathrm{D}t}\right) - 2\Omega_1\frac{\partial v}{\partial x} - 2\Omega_2\frac{\partial v}{\partial y} - 2\Omega_3\frac{\partial v}{\partial z} + 2\dot{\Omega}_2. \end{aligned}\right\} \tag{2.27}$$

3. Reduction of the pressure gradient

The key to the derivation of the surface equations in three dimensions (see (1.1)) is the precise treatment of the pressure field. Let

$$\beta(x,y,t) = -\dot{\Omega}_1(y+d_2)+\dot{\Omega}_2(x+d_1)-\Omega_3\Omega_1(x+d_1)-\Omega_3\Omega_2(y+d_2)-\boldsymbol{Q}\boldsymbol{e}_3\cdot\ddot{\boldsymbol{q}}-g\boldsymbol{Q}\boldsymbol{e}_3\cdot\boldsymbol{e}_3. \tag{3.1}$$

Then the vertical momentum equation can be expressed in the form

$$\frac{\mathrm{D}w}{\mathrm{D}t} + \frac{1}{\rho}\frac{\partial p}{\partial z} = -2(\Omega_1 v - \Omega_2 u) + \left(\Omega_1^2+\Omega_2^2\right)(z+d_3) + \beta(x,y,t). \tag{3.2}$$

Integrate from z to h,

$$\begin{aligned} \int_z^h \frac{\mathrm{D}w}{\mathrm{D}t}\,\mathrm{d}s + \frac{1}{\rho}p\Big|_z^h &= -2\Omega_1\int_z^h v\,\mathrm{d}s + 2\Omega_2\int_z^h u\,\mathrm{d}s \\ &\quad + \left(\Omega_1^2+\Omega_2^2\right)\left(\tfrac{1}{2}h^2 - \tfrac{1}{2}z^2 + d_3h - d_3z\right) + \beta(x,y,t)(h-z). \end{aligned} \tag{3.3}$$

Applying the surface boundary condition on the pressure then gives the pressure at any point z:

$$\frac{1}{\rho}p(x,y,z,t)=\int_z^h\frac{\mathrm{D}w}{\mathrm{D}t}\,\mathrm{d}s+2\Omega_1\int_z^h v\,\mathrm{d}s-2\Omega_2\int_z^h u\,\mathrm{d}s-\beta(x,y,t)(h-z)\\-\left(\Omega_1^2+\Omega_2^2\right)\left(\tfrac{1}{2}h^2-\tfrac{1}{2}z^2+d_3h-d_3z\right)-\sigma\,\mathrm{div}(\boldsymbol{\kappa}).\quad(3.4)$$

This equation for $p(x,y,z,t)$ is exact. The strategy is to take derivatives with respect to x and y and then substitute into the horizontal momentum equations. The details are lengthy and are given in Appendix A. The expressions are

$$\frac{1}{\rho}\frac{\partial p}{\partial x}=\frac{\mathrm{D}u}{\mathrm{D}t}\bigg|_z^h+\frac{\mathrm{D}w}{\mathrm{D}t}\bigg|^h h_x+2\Omega_2W-2\Omega_3V+2\dot{\Omega}_2(h-z)-2\Omega_2w+2\Omega_3v+2\Omega_1Vh_x\\-2\Omega_2Uh_x-\left(\Omega_1^2+\Omega_2^2\right)(h+d_3)h_x-\beta_x(h-z)-\beta h_x-\sigma\,\partial_x\,\mathrm{div}(\boldsymbol{\kappa}),\quad(3.5)$$

and

$$\frac{1}{\rho}\frac{\partial p}{\partial y}=\frac{\mathrm{D}v}{\mathrm{D}t}\bigg|_z^h+\frac{\mathrm{D}w}{\mathrm{D}t}\bigg|^h h_y-2\Omega_1W+2\Omega_3U-2\dot{\Omega}_1(h-z)+2\Omega_1w-2\Omega_3u+2\Omega_1Vh_y\\-2\Omega_2Uh_y-\left(\Omega_1^2+\Omega_2^2\right)(h+d_3)h_y-\beta_y(h-z)-\beta h_y-\sigma\,\partial_y\,\mathrm{div}(\boldsymbol{\kappa}).\quad(3.6)$$

The pressure is eliminated from the horizontal momentum equations using (3.5) and (3.6). The details will be given for the x-momentum equation and then the result will be stated for the y-momentum equation.

4. Reduction of the horizontal momentum equation

The x-component of the momentum equations (2.8) is

$$\frac{\mathrm{D}u}{\mathrm{D}t}+\frac{1}{\rho}\frac{\partial p}{\partial x}=-2(\Omega_2w-\Omega_3v)-\dot{\Omega}_2(z+d_3)+\dot{\Omega}_3(y+d_2)\\-\Omega_1\,\boldsymbol{\Omega}\cdot(\boldsymbol{x}+\boldsymbol{d})+(x+d_1)\|\boldsymbol{\Omega}\|^2-\mathbf{Q}\boldsymbol{e}_1\cdot\ddot{\boldsymbol{q}}-g\mathbf{Q}\boldsymbol{e}_1\cdot\boldsymbol{e}_3.\quad(4.1)$$

Replace the second term on the left-hand side by the expression for $\rho^{-1}p_x$ in (3.5),

$$\frac{\mathrm{D}u}{\mathrm{D}t}+\frac{\mathrm{D}u}{\mathrm{D}t}\bigg|_z^h+\frac{\mathrm{D}w}{\mathrm{D}t}\bigg|^h h_x=-2\Omega_2W+2\Omega_3V-2\dot{\Omega}_2(h-z)-2\Omega_1Vh_x+2\Omega_2Uh_x\\+2\Omega_2w-2\Omega_3v+\left(\Omega_1^2+\Omega_2^2\right)(h+d_3)h_x+\beta_x(h-z)+\beta h_x\\+\sigma\,\partial_x\mathrm{div}(\boldsymbol{\kappa})-2(\Omega_2w+\Omega_3v)-\dot{\Omega}_2(z+d_3)+\dot{\Omega}_3(y+d_2)\\-\Omega_1\,\boldsymbol{\Omega}\cdot(\boldsymbol{x}+\boldsymbol{d})+(x+d_1)\|\boldsymbol{\Omega}\|^2-\mathbf{Q}\boldsymbol{e}_1\cdot\ddot{\boldsymbol{q}}-g\mathbf{Q}\boldsymbol{e}_1\cdot\boldsymbol{e}_3.\quad(4.2)$$

There are convenient cancellations: principally, $\mathrm{D}u/\mathrm{D}t$, $2\dot{\Omega}_2z$ and the interior Coriolis terms cancel out. Cancelling and using $\beta_x=\dot{\Omega}_2-\Omega_1\Omega_3$, and the kinematic condition $W=h_t+Uh_x+Vh_y$ gives

$$\frac{\mathrm{D}u}{\mathrm{D}t}\bigg|^h+\frac{\mathrm{D}w}{\mathrm{D}t}\bigg|^h h_x+2\Omega_2(h_t+Uh_x+Vh_y)-2\Omega_3V+2\Omega_1Vh_x-2\Omega_2Uh_x\\-\left(\Omega_1^2+\Omega_2^2\right)(h+d_3)h_x-\left(\Omega_2^2+\Omega_3^2\right)(x+d_1)+\Omega_1\Omega_2(y+d_2)+\Omega_1\Omega_3(h+d_3)\\+\dot{\Omega}_2(h+d_3)-\dot{\Omega}_3(y+d_2)+\mathbf{Q}\boldsymbol{e}_1\cdot\ddot{\boldsymbol{q}}+g\mathbf{Q}\boldsymbol{e}_1\cdot\boldsymbol{e}_3-\beta h_x-\sigma\,\partial_x\mathrm{div}(\boldsymbol{\kappa})=0.\quad(4.3)$$

Now use the fact that $\mathrm{D}u/\mathrm{D}t|^h$ can be expressed purely in terms of surface variables since

$$U_t + UU_x + VU_y = \left.\frac{\mathrm{D}u}{\mathrm{D}t}\right|^h. \tag{4.4}$$

Substitution into (4.3) reduces the x-momentum equation to an equation purely in terms of surface variables

$$U_t + UU_x + VU_y + \left(a_{11} + \left.\frac{\mathrm{D}w}{\mathrm{D}t}\right|^h\right) h_x + a_{12}\, h_y = b_1 + \sigma\, \partial_x \mathrm{div}(\boldsymbol{\kappa}). \tag{4.5}$$

The coefficients in this equation are

$$\begin{aligned} a_{11}(x, y, t) &= 2\Omega_1 V - \left(\Omega_1^2 + \Omega_2^2\right)(h + d_3) - \beta \\ &= 2\Omega_1 V + \mathbf{Q}\boldsymbol{e}_3 \cdot \ddot{\boldsymbol{q}} + g\mathbf{Q}\boldsymbol{e}_3 \cdot \boldsymbol{e}_3 - \left(\Omega_1^2 + \Omega_2^2\right)(h + d_3) \\ &\quad -(\dot{\Omega}_2 - \Omega_1\Omega_3)(x + d_1) + (\dot{\Omega}_1 + \Omega_3\Omega_2)(y + d_2), \end{aligned} \tag{4.6}$$

$$a_{12} = 2\Omega_2 V, \tag{4.7}$$

and

$$\begin{aligned} b_1(x, y, t) = -2\Omega_2 h_t + 2\Omega_3 V - \mathbf{Q}\boldsymbol{e}_1 \cdot \ddot{\boldsymbol{q}} - g\mathbf{Q}\boldsymbol{e}_1 \cdot \boldsymbol{e}_3 + \left(\Omega_2^2 + \Omega_3^2\right)(x + d_1) \\ + (\dot{\Omega}_3 - \Omega_1\Omega_2)(y + d_2) - (\dot{\Omega}_2 + \Omega_1\Omega_3)(h + d_3). \end{aligned} \tag{4.8}$$

A similar argument leads to the surface y-momentum equation

$$V_t + UV_x + VV_y + a_{21}\, h_x + \left(a_{22} + \left.\frac{\mathrm{D}w}{\mathrm{D}t}\right|^h\right) h_y = b_2 + \sigma\, \partial_y \mathrm{div}(\boldsymbol{\kappa}), \tag{4.9}$$

with

$$a_{21} = -2\Omega_1 U, \tag{4.10}$$

and

$$\begin{aligned} a_{22} = -2\Omega_2 U - \left(\Omega_1^2 + \Omega_2^2\right)(h + d_3) + \mathbf{Q}\boldsymbol{e}_3 \cdot \ddot{\boldsymbol{q}} + g\mathbf{Q}\boldsymbol{e}_3 \cdot \boldsymbol{e}_3 \\ + (\dot{\Omega}_1 + \Omega_2\Omega_3)(y + d_2) - (\dot{\Omega}_2 - \Omega_1\Omega_3)(x + d_1), \end{aligned} \tag{4.11}$$

and

$$\begin{aligned} b_2 = 2\Omega_1 h_t - 2\Omega_3 U - \mathbf{Q}\boldsymbol{e}_2 \cdot \ddot{\boldsymbol{q}} - g\mathbf{Q}\boldsymbol{e}_2 \cdot \boldsymbol{e}_3 + \left(\Omega_1^2 + \Omega_3^2\right)(y + d_2) \\ - (\dot{\Omega}_3 + \Omega_1\Omega_2)(x + d_1) + (\dot{\Omega}_1 - \Omega_2\Omega_3)(h + d_3). \end{aligned} \tag{4.12}$$

The terms a_{11} and a_{22} are related by

$$a_{11} - 2\Omega_1 V = a_{22} + 2\Omega_2 U. \tag{4.13}$$

The surface equations (4.5) and (4.9) are exact. Moreover, the assumption of finite depth has not been used yet and so they are also valid in infinite depth. In order to reduce them to a closed system, the only term that requires modelling is the Lagrangian vertical acceleration at the surface, $\mathrm{D}w/\mathrm{D}t|^h$.

5. Penney–Price–Taylor theory for the highest standing wave

Before proceeding to reduce the surface equations to a closed set of SWEs, a key property of the exact equations is highlighted.

One of the simplest forms of sloshing waves is the pure standing wave. It is periodic in both space and time. Penney & Price (1952) argue that the *highest* 2-D standing wave should occur when the Lagrangian vertical acceleration at the crest is equal to $-g$. They consider standing waves in infinite depth only, but it will be clear from the discussion below that their argument is also valid in finite depth. Their argument – in the absence of surface tension – is that the pressure just inside the liquid near the surface must be positive or zero and consequently at the surface $\partial p/\partial z \leqslant 0$, which is equivalent to

$$g + \frac{\mathrm{D}w}{\mathrm{D}t}\bigg|^{h} \geqslant 0. \tag{5.1}$$

When this condition is violated, the standing wave should cease to exist. Taking into account that $\mathrm{D}w/\mathrm{D}t = \partial w/\partial t$ at a crest, this is equivalent to (67) in Penney & Price (1952). Using this theory, they deduced that the crest angle of the highest wave must be 90°, in contrast to the 120° angle of travelling waves. Taylor (1953) was surprised by this argument and tested it by constructing an experiment. He was mainly interested in the crest angle. His experiments convincingly confirmed the conjecture of Penney & Price (1952).

A theoretical justification of this theory can be deduced from the surface momentum equations. For the case of 2-D waves, this argument has been presented in § 6 of Alemi Ardakani & Bridges (2009*a*). Remarkably, this argument carries over to 3-D waves. Neglecting surface tension, and assuming the vessel to be stationary, the surface momentum equations (4.5) and (4.9) reduce to

$$\left.\begin{aligned} U_t + UU_x + VU_y + \left(g + \frac{\mathrm{D}w}{\mathrm{D}t}\bigg|^{h}\right) h_x = 0, \\ V_t + UV_x + VV_y + \left(g + \frac{D w}{\mathrm{D}t}\bigg|^{h}\right) h_y = 0. \end{aligned}\right\} \tag{5.2}$$

When $g + \mathrm{D}w/\mathrm{D}t|^{h} = 0$, these equations further reduce to

$$\left.\begin{aligned} U_t + UU_x + VU_y = 0, \\ V_t + UV_x + VV_y = 0. \end{aligned}\right\} \tag{5.3}$$

These equations are closed and indeed it is shown by Pomeau *et al.* (2008*a*) that they have an exact similarity solution. Moreover, this similarity solution gives a form of wave breaking, which has, in turn, been confirmed by numerical experiments in Pomeau *et al.* (2008*b*). The theoretical argument in Pomeau *et al.* (2008*a*) is by analogy with the SWEs but it is shown to be precise in Bridges (2009). This theory indicates that any 3-D standing waves will be susceptible to some form of breaking when the condition (5.1) is violated. Indeed, photographs of the experiments of Taylor (1953) show a form of crest instability near the highest standing wave – in the 2-D case, and his experiments also show a tendency to 3-D near the highest wave. See also figure 8(*c*) in Kobine (2008), which shows 3-D standing waves reaching a maximum. Adding in surface tension and a rotating frame will add new features to the theory.

Surface tension will likely provide a smoothing effect, but rotation will likely lead to a more complicated scenario for breaking.

In this paper, we are interested in shallow-water sloshing. In this case, it is natural to assume that the Lagrangian vertical accelerations at the surface are small, and so we will be working predominantly in the region where the condition (5.1) is strongly satisfied.

6. Conservation of mass

The vertical average of the horizontal velocity $(\overline{u}(x, y, t), \overline{v}(x, y, t))$ is defined by

$$\overline{u} := \frac{1}{h}\int_0^h u(x, y, z, t)\,\mathrm{d}z \quad \text{and} \quad \overline{v} := \frac{1}{h}\int_0^h v(x, y, z, t)\,\mathrm{d}z. \tag{6.1}$$

On differentiating, we get

$$\begin{aligned} h_t + (h\overline{u})_x + (h\overline{v})_y &= h_t + h_x u\Big|^h + \int_0^h u_x\,\mathrm{d}z + h_y v\Big|^h + \int_0^h v_y\,\mathrm{d}z \\ &= h_t + Uh_x + Vh_y + \int_0^h (u_x + v_y + w_z)\,\mathrm{d}z - \int_0^h w_z\,\mathrm{d}z \\ &= h_t + Uh_x + Vh_y - W + w\Big|_{z=0} \\ &= 0, \end{aligned} \tag{6.2}$$

using $u_x + v_y + w_z = 0$, the bottom boundary condition and the kinematic free-surface boundary condition. Hence, if $(\overline{u}, \overline{v})$ are used for the horizontal velocity field, then the h-equation in the SWEs in the form

$$h_t + (h\overline{u})_x + (h\overline{v})_y = 0 \tag{6.3}$$

is exact.

However, we are interested in an h-equation based on the surface horizontal velocity field. The surface and average velocities are related by

$$\left.\begin{aligned} U(x, y, t) - \overline{u}(x, y, t) &= \frac{1}{h}\int_0^h z u_z\,\mathrm{d}z, \\ V(x, y, t) - \overline{v}(x, y, t) &= \frac{1}{h}\int_0^h z v_z\,\mathrm{d}z. \end{aligned}\right\} \tag{6.4}$$

Use these identities to formulate the mass equation in terms of the surface velocity field. Differentiating (6.4) and using mass conservation, we get

$$\frac{\partial}{\partial x}\left[h(U - \overline{u})\right] + \frac{\partial}{\partial y}\left[h(V - \overline{v})\right] = W + hU_x + hV_y. \tag{6.5}$$

Replace W by the kinematic condition,

$$(h(U - \overline{u}))_x + (h(V - \overline{v}))_y = W + h(U_x + V_y) = h_t + (hU)_x + (hV)_y. \tag{6.6}$$

The error in using the surface velocity field in the h-equation can be characterized in two ways:

$$W + h(U_x + V_y) \approx 0 \quad \text{or} \quad (h(U - \overline{u}))_x + (h(V - \overline{v}))_y \approx 0. \tag{6.7}$$

7. SWEs for 3-D sloshing in a rotating vessel

To summarize, the candidate pre-SWEs for (h, U, V) are

$$\left.\begin{aligned} h_t + (hU)_x + (hV)_y &= W + hU_x + hV_y, \\ U_t + UU_x + VU_y + \left(a_{11} + \frac{\mathrm{D}w}{\mathrm{D}t}\Big|^h\right) h_x + a_{12}\, h_y &= b_1 + \sigma\, \partial_x \mathrm{div}(\boldsymbol{\kappa}), \\ V_t + UV_x + VV_y + a_{21}\, h_x + \left(a_{22} + \frac{\mathrm{D}w}{\mathrm{D}t}\Big|^h\right) h_y &= b_2 + \sigma\, \partial_y \mathrm{div}(\boldsymbol{\kappa}). \end{aligned}\right\} \tag{7.1}$$

The equation for W can be added as follows:

$$W_t + UW_x + VW_y = \frac{\mathrm{D}w}{\mathrm{D}t}\Big|^h. \tag{7.2}$$

The system (7.1) with or without (7.2) is not closed. If $\mathrm{D}w/\mathrm{D}t|^h$ is specified, then the system of four equations (7.1)–(7.2) for (h, U, V, W) is closed. This system of four equations can be further reduced to a system of three equations with an additional assumption on the surface vertical velocity.

Henceforth, it is assumed that the vertical velocity at the free surface satisfies

$$|W + hU_x + hV_y| \ll 1, \tag{7.3}$$

and the Lagrangian vertical acceleration at the free surface satisfies

$$\left|\frac{\mathrm{D}w}{\mathrm{D}t}\Big|^h\right| \ll |a_{11}| \quad \text{and} \quad \left|\frac{\mathrm{D}w}{\mathrm{D}t}\Big|^h\right| \ll |a_{22}|. \tag{7.4}$$

The assumption (7.3) has an alternative characterization, as shown in (6.7). For small vessel motion, the second assumption (i.e. (7.4)) is equivalent to assuming that the Lagrangian vertical accelerations are small compared with the gravitational acceleration.

The coefficients of h_x and h_y can lead to instability and even loss of well-posedness. Let

$$\boldsymbol{A} = \begin{pmatrix} a_{11} & a_{12} \\ a_{21} & a_{22} \end{pmatrix}, \tag{7.5}$$

and define

$$\mathrm{sym}(\boldsymbol{A}) := \tfrac{1}{2}(\boldsymbol{A} + \boldsymbol{A}^{\mathrm{T}}), \tag{7.6}$$

the symmetric part of $\boldsymbol{A}$. Then the following assumption is imposed on the coefficients:

$$\mathrm{sym}(\boldsymbol{A}) \quad \text{is positive definite.} \tag{7.7}$$

This condition is deduced from the following linear constant-coefficient problem:

$$\left.\begin{aligned} h_t + h_0(U_x + V_y) &= 0, \\ U_t + a_{11}h_x + a_{12}h_y &= 0, \\ V_t + a_{21}h_x + a_{22}h_y &= 0. \end{aligned}\right\} \tag{7.8}$$

Differentiating and combining gives the following wave equation for $h(x, y, t)$:

$$h_{tt} = h_0(a_{11}h_{xx} + (a_{12} + a_{21})h_{xy} + a_{22}h_{yy}). \tag{7.9}$$

The condition (7.7) is precisely the condition for this wave equation to be well-posed. This condition eliminates anomalies such as vertical downward accelerations

exceeding gravity, and rotating or spinning motion leading to overturning of the vessel.

7.1. *Restrictions on the rigid-body motion*

The principal restrictions on the rigid-body motion are the induced restriction that is implicit in the global condition (7.4), through a_{11} and a_{22}, and the local condition (7.7) through matrix $\boldsymbol{A}$.

In individual cases, the restrictions on the rigid-body motion can be made precise. For example, in pure yaw motion, considered in § 13, there is no restriction on the vertical angular velocity (other than the restriction on the induced fluid motion). Section 7.3 discusses limits on the rigid-body motion induced by a particular shallow-water scaling.

Another case where one can be precise, and is illuminating, is to assume that the vehicle is prescribed to move on the surface of a sphere. This motion can be produced by taking $\boldsymbol{Q} = \boldsymbol{I}$ and

$$\boldsymbol{q}(t) = (q_1(t), q_2(t), q_3(t)) = R(\cos\theta(t)\cos\phi(t), \cos\theta(t)\sin\phi(t), \sin\theta(t)), \tag{7.10}$$

with R being the radius of the sphere, $\phi(t)$ an arbitrary function of time and

$$\theta(t) = \omega t \quad \text{with} \quad \omega \text{ constant}. \tag{7.11}$$

In this case,

$$a_{11} = a_{22} = g - \omega^2 R\sin\theta, \quad a_{12} = a_{21} = 0. \tag{7.12}$$

Hence, the assumption (7.7) requires that

$$\omega < \sqrt{\frac{g}{R}}. \tag{7.13}$$

Mathematically, the SWEs become ill-posed when this condition is exceeded. Physically, the centripetal acceleration is exceeding the gravitational acceleration. A special case of the above vessel motion, where the vessel lies on a great circle on the sphere, is considered in § 15.

7.2. *Neglect of surface tension*

Under the assumptions (7.3) and (7.4) and under the additional assumption that $\sigma = 0$ (neglect of surface tension), the SWEs are hyperbolic. When $\sigma \neq 0$, they are dispersive, for in that case

$$\mathrm{div}(\boldsymbol{\kappa}) = \frac{\partial \kappa_1}{\partial x} + \frac{\partial \kappa_2}{\partial y} = h_{xx} + h_{yy} + \cdots, \tag{7.14}$$

where the dots correspond to nonlinear terms in h and its derivatives. Hence, the σ terms on the right-hand side of (U, V) equations in (7.1) have the form

$$\left.\begin{aligned} \partial_x \mathrm{div}(\boldsymbol{\kappa}) &= h_{xxx} + h_{yyx} + \cdots, \\ \partial_y \mathrm{div}(\boldsymbol{\kappa}) &= h_{xxy} + h_{yyy} + \cdots. \end{aligned}\right\} \tag{7.15}$$

At the linear level, these terms add dispersion to the SWEs. They will also require additional boundary conditions at the walls (cf. Billingham 2002; Kidambi & Shankar 2004), as a contact angle effect appears at the vessel walls. In this paper, we will primarily be concerned with long waves and so will henceforth neglect surface tension:

$$\sigma = 0. \tag{7.16}$$

7.3. *(7.3) and (7.4) in the shallow-water limit*

The conditions (7.3) and (7.4) are global. That is, there is no particular restriction on parameter values. Indeed, they may be satisfied even in deep water. However, the most natural regime where one would expect them to be satisfied is in the shallow-water regime. In this section, a scaling argument and asymptotics are used to analyse (7.3) and (7.4) in the shallow-water limit. The small parameter representing shallow water is

$$\varepsilon = \frac{h_0}{L}, \tag{7.17}$$

where L is a representative horizontal length scale. Let $U_0 = \sqrt{gh_0}$ be the representative horizontal velocity scale. Introduce the standard shallow-water scaling (e.g. p. 482 of Dingemans 1997),

$$\left.\begin{aligned} \widetilde{x} &= \frac{x}{L}, \quad \widetilde{y} = \frac{y}{L}, \quad \widetilde{z} = \frac{z}{h_0} = \frac{z}{\varepsilon L}, \quad \widetilde{t} = \frac{tU_0}{L}, \\ \widetilde{u} &= \frac{u}{U_0}, \quad \widetilde{v} = \frac{v}{U_0}, \quad \widetilde{w} = \frac{w}{\varepsilon U_0}, \quad \widetilde{h} = \frac{h}{h_0}. \end{aligned}\right\} \tag{7.18}$$

The scaled version of the surface velocities are denoted by $\widetilde{U}$, $\widetilde{V}$ and $\widetilde{W}$.

The typical strategy for deriving an asymptotic shallow-water model is to scale the full Euler equations, and then use an asymptotic argument to reduce the vertical pressure field and vertical velocities (e.g. § 5.1 of Dingemans 1997). Here, however, we have an advantage as the full Euler equations have been reduced to the exact surface equations (7.1). Hence, the strategy here is to start by scaling the exact equations (7.1) and then apply an asymptotic argument.

To check (7.3), start by scaling the exact mass equation in (7.1):

$$\widetilde{h}_{\widetilde{t}} + (\widetilde{h}\widetilde{U})_{\widetilde{x}} + (\widetilde{h}\widetilde{V})_{\widetilde{y}} = \widetilde{W} + \widetilde{h}(\widetilde{U}_{\widetilde{x}} + \widetilde{V}_{\widetilde{y}}). \tag{7.19}$$

At first glance, it appears that the left-hand side and the right-hand side are of the same order, since ε does not appear. However, the *sum* on the right-hand side is of higher order. The fact that the right-hand side is of higher order is intuitively clear, since it can be expressed (see (6.6)) in terms of the velocity differences $U-\overline{u}$ and $V-\overline{v}$ and, in the shallow-water approximation, the horizontal surface velocities (U, V) and average velocities $(\overline{u}, \overline{v})$ are asymptotically equivalent. However, to make this precise, we need to bring in the vorticity field.

Go back to the unscaled mass equation and rewrite the right-hand side using (6.6) and (6.4):

$$h_t + (hU)_x + (hV)_y = \frac{\partial}{\partial x}\left(\int_0^h z u_z \,\mathrm{d}z\right) + \frac{\partial}{\partial y}\left(\int_0^h z v_z \,\mathrm{d}z\right). \tag{7.20}$$

Substitute for u_z and v_z using the vorticity field (2.23) as follows:

$$h_t + (hU)_x + (hV)_y = \frac{\partial}{\partial x}\left(\int_0^h z\,(\mathcal{V}_2 + w_x)\,\mathrm{d}z\right) + \frac{\partial}{\partial y}\left(\int_0^h z\,(w_y - \mathcal{V}_1)\,\mathrm{d}z\right). \tag{7.21}$$

This equation is exact. The key to showing that the right-hand side is of higher order is the scaling of the vorticity. The appropriate scaling is to assume that *the vorticity is asymptotically vertical*:

$$(\mathcal{V}_1, \mathcal{V}_2, \mathcal{V}_3) = \frac{U_0}{L}(\varepsilon\widetilde{\mathcal{V}}_1, \varepsilon\widetilde{\mathcal{V}}_2, \widetilde{\mathcal{V}}_3). \tag{7.22}$$

This property of vorticity is implicit in the classical shallow-water theory, and here it is made explicit.

Scaling (7.21) then gives

$$\widetilde{h}_{\widetilde{t}} + (\widetilde{h}\widetilde{U})_{\widetilde{x}} + (\widetilde{h}\widetilde{V})_{\widetilde{y}} = \varepsilon^2 \Delta(x, y, t, \varepsilon), \tag{7.23}$$

where

$$\Delta = \frac{\partial}{\partial \widetilde{x}} \int_0^{\widetilde{h}} \widetilde{z} \left(\widetilde{\mathcal{V}}_2 + \frac{\partial \widetilde{w}}{\partial \widetilde{x}} \right) \mathrm{d}\widetilde{z} + \frac{\partial}{\partial \widetilde{y}} \int_0^{\widetilde{h}} \widetilde{z} \left(-\widetilde{\mathcal{V}}_1 + \frac{\partial \widetilde{w}}{\partial \widetilde{y}} \right) \mathrm{d}\widetilde{z}. \tag{7.24}$$

Taking the limit $\varepsilon \to 0$ shows that (7.3) is satisfied. However, to be precise, it is essential that

$$\Delta(x, y, t, \varepsilon) \quad \text{is bounded in the limit } \varepsilon \to 0. \tag{7.25}$$

Assumption (7.4) requires that the vertical acceleration in the two terms,

$$\left(a_{11} + \frac{\mathrm{D}w}{\mathrm{D}t}\bigg|^h \right) \quad \text{and} \quad \left(a_{22} + \frac{\mathrm{D}w}{\mathrm{D}t}\bigg|^h \right), \tag{7.26}$$

in (7.1) be small, relative to magnitudes of a_{11} and a_{22}. After scaling, the Lagrangian vertical acceleration in the interior becomes

$$\frac{\mathrm{D}w}{\mathrm{D}t} = \varepsilon \frac{U_0^2}{L} \left(\frac{\partial \widetilde{w}}{\partial \widetilde{t}} + \widetilde{u} \frac{\partial \widetilde{w}}{\partial \widetilde{x}} + \widetilde{v} \frac{\partial \widetilde{w}}{\partial \widetilde{y}} + \widetilde{w} \frac{\partial \widetilde{w}}{\partial \widetilde{z}} \right) := \varepsilon \frac{U_0^2}{L} \frac{\mathrm{D}\widetilde{w}}{\mathrm{D}\widetilde{t}}. \tag{7.27}$$

Hence,

$$\frac{\mathrm{D}w}{\mathrm{D}t}\bigg|^h = \varepsilon \frac{U_0^2}{L} \frac{\mathrm{D}\widetilde{w}}{\mathrm{D}\widetilde{t}}\bigg|^{\widetilde{h}} = g\varepsilon^2 \frac{\mathrm{D}\widetilde{w}}{\mathrm{D}\widetilde{t}}\bigg|^{\widetilde{h}}, \tag{7.28}$$

using $U_0^2 = gh_0 = gL\varepsilon$. The scaled version of the first term in (7.26) is therefore

$$\left(a_{11} + \frac{\mathrm{D}w}{\mathrm{D}t}\bigg|^h \right) = g \left(\frac{a_{11}}{g} + \varepsilon^2 \frac{\mathrm{D}\widetilde{w}}{\mathrm{D}\widetilde{t}}\bigg|^{\widetilde{h}} \right), \tag{7.29}$$

with a similar expression for the a_{22} term.

In the shallow-water regime, the assumption (7.4) is satisfied if

$$\frac{a_{11}}{g} \quad \text{and} \quad \frac{a_{22}}{g} \quad \text{are of order one and} \quad \left| \frac{D\widetilde{w}}{D\widetilde{t}}\bigg|^{\widetilde{h}} \right| \quad \text{is bounded as} \quad \varepsilon \to 0. \tag{7.30}$$

However, by introducing scaling and taking an asymptotic limit, other anomalies can be introduced. We have to ensure that b_1 and b_2 are of the same order – or of higher order – as the left-hand side of the second and third equations of (7.1). Look at the second equation with surface tension neglected:

$$U_t + UU_x + VU_y + \left(a_{11} + \frac{\mathrm{D}w}{\mathrm{D}t}\bigg|^h \right) h_x + a_{12} h_y = b_1. \tag{7.31}$$

The left-hand side scales like $U_0^2/L = g\varepsilon$. With the standard scaling for $\boldsymbol{\Omega}$,

$$(\Omega_1, \Omega_2, \Omega_3) = \frac{U_0}{L} (\widetilde{\Omega}_1, \widetilde{\Omega}_2, \widetilde{\Omega}_3), \tag{7.32}$$

all the terms in b_1 in (4.8) are of order ε or higher except for the term $g\boldsymbol{Q}\boldsymbol{e}_1 \cdot \boldsymbol{e}_3$, which is of order unity. In scaled variables, it will be of order ε^{-1}. Hence, this scaling puts

a restriction on the angular velocity. A natural scaling that renders b_1 consistent is to take the angular velocity to be asymptotically vertical, like the vorticity:

$$(\Omega_1, \Omega_2, \Omega_3) = \frac{U_0}{L}(\varepsilon\widetilde{\Omega}_1, \varepsilon\widetilde{\Omega}_2, \widetilde{\Omega}_3). \tag{7.33}$$

To verify that b_1 is now consistent, it is necessary to show that

$$\lim_{\varepsilon\to 0}\frac{1}{\varepsilon}\boldsymbol{Q}(\widetilde{t},\varepsilon)\boldsymbol{e}_1\cdot\boldsymbol{e}_3 \quad \text{is of order unity (or higher in } \varepsilon). \tag{7.34}$$

This property follows from the scaling (7.33). In scaled variables, $\boldsymbol{Q}(\widetilde{t},\varepsilon)$ satisfies

$$\frac{\mathrm{d}}{\mathrm{d}\widetilde{t}}\boldsymbol{Q} = \boldsymbol{Q}\widetilde{\widetilde{\boldsymbol{\Omega}}}, \quad \widetilde{\widetilde{\boldsymbol{\Omega}}} = \begin{bmatrix} 0 & -\widetilde{\Omega}_3 & \varepsilon\widetilde{\Omega}_2 \\ \widetilde{\Omega}_3 & 0 & -\varepsilon\widetilde{\Omega}_1 \\ -\varepsilon\widetilde{\Omega}_2 & \varepsilon\widetilde{\Omega}_1 & 0 \end{bmatrix}. \tag{7.35}$$

(See (2.3) for the unscaled version.) Hence, in the limit as $\varepsilon \to 0$,

$$\lim_{\varepsilon\to 0}\boldsymbol{Q}(\widetilde{t},\varepsilon) := \boldsymbol{Q}(\widetilde{t},0) = \begin{bmatrix} \cos\psi(\widetilde{t}) & -\sin\psi(\widetilde{t}) & 0 \\ \sin\psi(\widetilde{t}) & \cos\psi(\widetilde{t}) & 0 \\ 0 & 0 & 1 \end{bmatrix}, \quad \text{where} \quad \frac{\mathrm{d}\psi}{\mathrm{d}\widetilde{t}} = \widetilde{\Omega}_3, \tag{7.36}$$

and

$$\boldsymbol{Q}(\widetilde{t},0)\boldsymbol{e}_1\cdot\boldsymbol{e}_3 = 0, \tag{7.37}$$

confirming that $\boldsymbol{Q}(\widetilde{t},\varepsilon)\boldsymbol{e}_1\cdot\boldsymbol{e}_3 = \mathcal{O}(\varepsilon)$ as $\varepsilon \to 0$. A similar argument shows that the term $\boldsymbol{Q}(\widetilde{t},\varepsilon)\boldsymbol{e}_2\cdot\boldsymbol{e}_3 = \mathcal{O}(\varepsilon)$ as $\varepsilon \to 0$, which appears in b_2.

The above scaling is only one of many, even in the shallow-water limit. A study of the various asymptotic regimes is outside the scope of this paper. Our main guide is the two meta-assumptions (i.e. (7.3) and (7.4)). They are required, in general, for closure and will have to be satisfied by any choice of scaling.

On the other hand, the above shallow-water scaling does appear implicitly in the numerical results. We have found that roll–pitch type forcing (i.e. Ω_1 and Ω_2 non-zero) requires very small amplitude in order to avoid large fluid motions that would violate (7.3) and/or (7.4), whereas the amplitude of yaw (Ω_3 non-zero) can be much larger (e.g. § 13) and similarly the amplitude of translation ($\boldsymbol{q}$) can be of order unity (e.g. § 15).

8. Potential vorticity for the SWEs with 3-D rotations

The classical SWEs conserve PV, which is the vertical vorticity divided by the depth: $h^{-1}(V_x - U_y)$, and the classical rotating SWEs in geophysical fluid dynamics conserve the perturbed quantity $h^{-1}(V_x - U_y + 2f)$, where the angular velocity vector is $\boldsymbol{\Omega} = (0, 0, f)$ (see § 4.2 of Salmon 1998).

The new surface SWEs conserve a form of PV which generalizes the classical case in an illuminating way. We have discovered that the SWEs conserve the form of PV introduced in (1.5). The second term in the numerator can be interpreted geometrically. Using the normal vector $\boldsymbol{n}$ at the free surface defined in (2.22), the expression for PV is

$$\mathrm{PV} = \frac{V_x - U_y + 2\ell\boldsymbol{n}\cdot\boldsymbol{\Omega}}{h}. \tag{8.1}$$

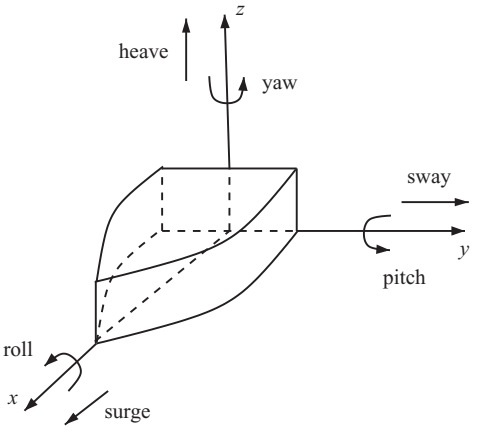

FIGURE 2. Diagram showing conventions for roll, pitch, yaw, surge, sway and heave.

In this expression, $\boldsymbol{\Omega}$ is the body representation of the angular velocity. If the spatial representation of the angular velocity is used (e.g. viewed from a laboratory frame), the form of PV is

$$\mathrm{PV} = \frac{V_x - U_y + 2\ell \boldsymbol{Qn} \cdot \boldsymbol{\Omega}^{spatial}}{h}. \tag{8.2}$$

Note that PV is not changed between (8.1) and (8.2), but only the representation is changed. In Appendix B, it is proved that

$$\frac{\mathrm{D}}{\mathrm{D}t}(\mathrm{PV}) = 0. \tag{8.3}$$

In the classical SWEs, preservation of PV has many important consequences (see review of McIntyre 2003). The generalization of PV to SWEs with 3-D rotations presented above provides a setting for studying the implications of vorticity for shallow-water sloshing. In 2-D shallow water, the predominant wave is a travelling hydraulic jump, when the vessel is forced harmonically near resonance. In 3-D shallow water, with multi-component harmonic forcing, the potential for very complex dynamics of curved hydraulic jumps can be expected. These hydraulic jumps will have an impact on the vorticity budget.

For example, there is an interesting mechanism for the generation of vorticity due to a hydraulic jump in two (horizontal) space dimensions discovered by Pratt (1983) and Peregrine (1998, 1999). They give a formula for the amount of PV generated in the classical SWEs due to a discontinuous bore. However, *their work applies only to steady bores*. An extension of this theory to *unsteady* multi-dimensional hydraulic jumps would provide some insight into the role of vorticity in shallow-water sloshing.

9. Prescribing the rigid-body motion of the vessel

The fluid vessel is a rigid body free to undergo any motion in 3-D space. Every rigid-body motion in $\mathbb{R}^3$ is uniquely determined by $(\boldsymbol{q}(t), \boldsymbol{Q}(t))$, where $\boldsymbol{q}(t)$ is the three-component translation vector and $\boldsymbol{Q}(t)$ is an orthogonal matrix with unit determinant (cf. Chapter 7 of O'Reilly 2008). In terms of the body coordinates, the translations are surge, sway and heave, and the rotations are labelled roll, pitch and yaw, as illustrated in figure 2.

Translations are straightforward to prescribe and need no special attention other than to be careful about whether the spatial or body representation is used. In this paper, $\boldsymbol{q}(t)$ is the translation of the body relative to the spatial frame. If the translation is specified from onboard the vessel – that is, specifying the surge, sway and heave directly – then the accelerations are related by

$$\begin{pmatrix} \ddot{q}_1^{surge} \\ \ddot{q}_2^{sway} \\ \ddot{q}_3^{heave} \end{pmatrix} = \begin{bmatrix} Q_{11} & Q_{21} & Q_{31} \\ Q_{12} & Q_{22} & Q_{32} \\ Q_{13} & Q_{23} & Q_{33} \end{bmatrix} \begin{pmatrix} \ddot{q}_1 \\ \ddot{q}_2 \\ \ddot{q}_3 \end{pmatrix}. \tag{9.1}$$

Note that the matrix on the right is the transpose of the rotation matrix. The natural approach in the context of experiments is to specify the absolute translations along with the rotations. Although we are not aware of any experiments which combine both. The paper of Disimile *et al.* (2009) indicates that their experimental facility for sloshing has the capability to produce all six degrees of freedom in the forcing.

On the other hand, specification of the rotations requires some care. The set of orthogonal matrices is highly nonlinear and in $\mathbb{R}^3$ the rotation matrices are no longer commutative in general. The simplest way to specify a rotation is to use Euler angles. The properties of Euler angles needed in this paper are recorded in Appendix C. However, even here one must be careful because Euler-angle representations are inherently singular, and there are subtleties in the deduction of the appropriate angular velocity (Leubner 1981). It is also important to remember that Euler angles provide only a very special class of rotations. If, for example, the angular velocity vector of a vessel is specified arbitrarily, deducing the Euler-angle representation will be intractable in general.

The construction of $\boldsymbol{Q}(t)$ can also be approached directly using numerical integration. The rotation matrix satisfies

$$\dot{\boldsymbol{Q}} = \boldsymbol{Q}\widehat{\boldsymbol{\Omega}}, \quad \boldsymbol{Q}(0) = \boldsymbol{I}, \tag{9.2}$$

where $\widehat{\boldsymbol{\Omega}}$ is the matrix representation of the body angular velocity (2.3). This approach is most effective if the angular velocity is given. One setting where the body angular velocity is available is in strapdown inertial navigation systems (e.g. Chapter 11 of Titterton & Weston 2004). The navigation system outputs the body angular velocity and then (9.2) is solved numerically for $\boldsymbol{Q}(t)$ (called the attitude matrix in navigation literature).

Another efficient approach to constructing rotation matrices is the use of quaternions. Quaternions are now widely used in computer graphics algorithms (Hanson 2006) and in molecular dynamics (Evans 1977; Rapaport 1985). Evans (1977) points out that 'quaternion [computer] programmes seem to run ten times faster than corresponding [computer] programmes employing Euler angles'. However, in our case, the computing time for the rotations is very small compared to the computing time for the fluid motion, so the simpler approach of computing $\boldsymbol{Q}$ directly by integrating (9.2) is adapted.

The differential equation (9.2) can be integrated numerically very efficiently, although the choice of numerical integrator is very important as it is essential to maintain orthogonality to machine accuracy. An efficient second-order algorithm for (9.2) is the implicit midpoint rule (Leimkuhler & Reich 2004) with discretization,

$$\frac{\boldsymbol{Q}^{n+1} - \boldsymbol{Q}^n}{\Delta t} = \left(\frac{\boldsymbol{Q}^{n+1} + \boldsymbol{Q}^n}{2} \right) \widehat{\boldsymbol{\Omega}}(t^{n+1/2}), \tag{9.3}$$

where $\widehat{\boldsymbol{\Omega}}(t)$ is treated as given; rearranging yields

$$\boldsymbol{Q}^{n+1} = \boldsymbol{Q}^n + \tfrac{1}{2}\Delta t(\boldsymbol{Q}^{n+1} + \boldsymbol{Q}^n)\widehat{\boldsymbol{\Omega}}(t^{n+1/2}). \tag{9.4}$$

Setting

$$\boldsymbol{S}^{n+(1/2)} = \tfrac{1}{2}\Delta t\widehat{\boldsymbol{\Omega}}\left(t^{n+(1/2)}\right), \tag{9.5}$$

one time step is represented by

$$\boldsymbol{Q}^{n+1} = \boldsymbol{Q}^n\left(\boldsymbol{I} + \boldsymbol{S}^{n+(1/2)}\right)\left(\boldsymbol{I} - \boldsymbol{S}^{n+(1/2)}\right)^{-1}. \tag{9.6}$$

Since $\boldsymbol{S}^n$ is skew-symmetric, the term $(\boldsymbol{I} + \boldsymbol{S}^n)(\boldsymbol{I} - \boldsymbol{S}^n)^{-1}$ is orthogonal. Hence, orthogonality is preserved to machine accuracy at each time step.

When $\boldsymbol{\Omega}(t)$ is specified, this integration scheme can be designed to exactly synchronize with the time integration of the fluid equations.

The implicit midpoint rule is a special case of the Gauss–Legendre Runge–Kutta (GLRK) methods which have been shown to preserve orthogonality to machine accuracy, and they can be constructed to any order of accuracy (Leimkuhler & Reich 2004). There are other effective and efficient methods for integrating (9.2) and some recent developments are reviewed in Romero (2008).

9.1. *Linearizing rotations*

When using Euler angles with very small-amplitude forcing, the angular velocity is sometimes approximated by the derivative of the angles. For example, consider the case of the 3–2–1 Euler angles introduced in Appendix C. The body representation of the angular velocity is

$$\boldsymbol{\Omega} = \begin{pmatrix} \dot{\phi} - \dot{\psi}\sin\theta \\ \dot{\psi}\cos\theta\sin\phi + \dot{\theta}\cos\phi \\ \dot{\psi}\cos\theta\cos\phi - \dot{\theta}\sin\phi \end{pmatrix}. \tag{9.7}$$

Neglecting terms that are quadratic in the angles reduces this expression to

$$\boldsymbol{\Omega} \approx \begin{pmatrix} \dot{\phi} \\ \dot{\theta} \\ \dot{\psi} \end{pmatrix}. \tag{9.8}$$

This approximation is appealing, since $\boldsymbol{\Omega} = \dot{\Theta}$ and $\dot{\boldsymbol{\Omega}} = \ddot{\boldsymbol{\Theta}}$, with $\boldsymbol{\Theta} = (\phi, \theta, \psi)$. This linearization is also mathematically correct.

On the other hand, linearization of the associated rotation has to be done with care. The temptation is to approximate the rotation by

$$\boldsymbol{Q}^{approx} = \boldsymbol{I} + \widehat{\boldsymbol{\Theta}}, \quad \widehat{\boldsymbol{\Theta}} = \begin{pmatrix} 0 & -\psi & \theta \\ \psi & 0 & -\phi \\ -\theta & \phi & 0 \end{pmatrix}, \tag{9.9}$$

and this approximation is used in the literature. However, this approximation is no longer a rotation since

$$(\boldsymbol{Q}^{approx})^{\mathrm{T}} \neq (\boldsymbol{Q}^{approx})^{-1}. \tag{9.10}$$

It will still produce a motion of the vehicle, but not necessarily a physical motion, since the approximate rotation (9.9) is not bounded in general, and so, over long times, artificial displacements of the vehicle will arise.

An approximation, to the same order of accuracy, can be obtained using the Cayley transform

$$\boldsymbol{Q}^{Cayley} = \left(\boldsymbol{I} + \tfrac{1}{2}\widehat{\boldsymbol{\Theta}}\right)\left(\boldsymbol{I} - \tfrac{1}{2}\widehat{\boldsymbol{\Theta}}\right)^{-1}. \tag{9.11}$$

This matrix is orthogonal and has the same order of approximation as (9.9).

On the other hand, there is no reason to linearize the Euler angles in either analysis or in numerics. In general, it is best to use the exact expressions for the Euler angles, even for small angles. In this paper, only exact representations of the rotations are used. Indeed, as far as we are aware, the simulations of sloshing reported here are the first to use exact representations for 3-D rotations.

9.2. *Harmonic forcing*

Harmonic motion can be specified by expressing the Euler angles in terms of harmonic motion, or by arbitrarily specifying the angular velocity and then integrating (9.2) to obtain the rotation. For example, in the case of roll–pitch with the same phase, but different amplitudes and frequencies,

$$\phi(t) = \varepsilon_r \cos\omega_r t \quad \text{and} \quad \theta(t) = \varepsilon_p \cos\omega_p t. \tag{9.12}$$

In choosing the forcing frequency, it is not the value of the frequency that is important but its value relative to the natural frequency. In the limit of shallow water, the natural frequencies of the fluid are

$$\omega_{mn} = \pi\sqrt{gh_0}\left(\frac{m^2}{L_1^2} + \frac{n^2}{L_2^2}\right)^{1/2}, \quad m, n = 0, 1, 2, \ldots. \tag{9.13}$$

10. Review of previous derivations of rotating SWEs for sloshing

Two derivations of the SWEs for fluid in a vessel that is undergoing a general rigid-body motion in three dimensions first appeared in the literature at about the same time, given independently by Dillingham & Falzarano (1986) and Pantazopoulos (1987) (hereafter called the DFP SWEs). Both derivations follow the same strategy. An extensive review of their derivations is in Alemi Ardakani & Bridges (2009*c*). There are several key weaknesses in their derivation. Firstly, they use the *spatial* representation of the angular velocity. This choice, although not incorrect, leads to very complicated equations, which simplify dramatically simply by changing to the body representation. Secondly, they make a small-angle approximation and so the angular velocity reduces to the form

$$\boldsymbol{\Omega} = (\dot{\phi}, \dot{\theta}, 0), \tag{10.1}$$

similar to a 2-D rotation, where ϕ is the roll angle and θ is the pitch angle. Hence, the full structure of 3-D rotations is lost. They also restrict to roll–pitch motion. Thirdly, they make strong assumptions which approximate equations with potentially much larger error than the surface SWEs.

The velocity field (U, V) is not the same as the velocity field in the DFP SWEs. DFPs do not specify exactly which horizontal velocity they use but their h-equation becomes exact if the average horizontal velocity is used. In any case, assume for purposes of comparison that $(U, V) \approx (u, v)$, and then the coefficients in the two

systems can be compared,

$$\left.\begin{aligned} a_{11} &= a_{(z)} + 2\Omega_2 U - \left(\Omega_1^2 + \Omega_2^2\right)h - (\dot{\Omega}_2 - \Omega_1\Omega_3)d_1 + (\dot{\Omega}_1 + \Omega_2\Omega_3)d_2, \\ a_{12} &= a_{12}^{DFP} + 2\Omega_2 V, \quad a_{21} = a_{21}^{DFP} - 2\Omega_1 U, \\ a_{22} &= a_{(z)} - 2\Omega_1 V - \left(\Omega_1^2 + \Omega_2^2\right)h - (\dot{\Omega}_2 - \Omega_1\Omega_3)d_1 + (\dot{\Omega}_1 + \Omega_2\Omega_3)d_2. \end{aligned}\right\} \tag{10.2}$$

The right-hand-side coefficient comparison is

$$\left.\begin{aligned} b_1 &= f_1 - 2\Omega_2 h_t + \left(\Omega_2^2 + \Omega_3^2\right)d_1 + (\dot{\Omega}_3 - \Omega_1\Omega_2)d_2 - (\dot{\Omega}_2 + \Omega_1\Omega_3)h, \\ b_2 &= f_2 + 2\Omega_1 h_t + \left(\Omega_1^2 + \Omega_3^2\right)d_2 - (\dot{\Omega}_3 + \Omega_1\Omega_2)d_1 + (\dot{\Omega}_1 - \Omega_2\Omega_3)h. \end{aligned}\right\} \tag{10.3}$$

The d_1 and d_2 error terms are not so important since they could be included in the DFP formulation; so they can be discounted. The discrepancy between the two formulations is still quite significant when the rotation field is present. This discrepancy is due to the fact that the DFP SWEs have more assumptions than the surface SWEs. See the report of Alemi Ardakani & Bridges (2009*c*) for details.

Another strategy for deriving the SWEs for fluid in a vessel that is undergoing a general rigid-body motion in three dimensions has been proposed by Huang (1995) and Huang & Hsiung (1996, 1997). Their derivation is more precise, and starts with the full 3-D equations. A detailed report on their derivation is given in Alemi Ardakani & Bridges (2009*d*). They explicitly take $u(x, y, z, t)$ and $v(x, y, z, t)$ to be independent of z but implicitly they are using the average horizontal velocity field $(\overline{u}, \overline{v})$. They neglect the vertical acceleration in general (not just at the free surface) and integrate the vertical pressure gradient, differentiate and then substitute into the horizontal momentum equations.

To compare these HH SWEs with new surface equations, assume that the (U, V) velocity field in the surface equations is equivalent to the velocity field in the HH SWEs, and compare coefficients

$$\left.\begin{aligned} a_{11}^{HH} &= a_{11} - 2\Omega_2 U, \quad a_{22}^{HH} = a_{22} + 2\Omega_1 V, \\ a_{12}^{HH} &= a_{12} - 2\Omega_2 V, \quad a_{21}^{HH} = a_{21} + 2\Omega_1 U, \\ b_1^{HH} &= b_1 + 2\Omega_2 h_t + \dot{\Omega}_2 h, \quad b_2^{HH} = b_2 - 2\Omega_1 h_t - \dot{\Omega}_1 h. \end{aligned}\right\} \tag{10.4}$$

The agreement between the HH SWEs and the surface SWEs is much better than the case of the DFP SWEs but there are still important differences when Ω_1 and Ω_2 are important. One case where the surface equations and the HH SWEs agree exactly (assuming equivalence of the velocity fields) is when the forcing is pure yaw motion, and numerical experiments on this case are discussed in § 13.

Another source where 3-D SWEs in a rotating vessel appear is in Exercise 9.6.4 on p. 436 of Faltinsen & Timokha (2009). The exercise asks the reader to derive two forms of the SWEs in three dimensions in a rotating frame. The first part of the question leads to a derivation of the DFP equations (see part (*b*) on p. 436). It is an improvement over DFP in that the body representation for the angular velocity is used, but the angular velocity is linearized. In the second part of the question, the reader is asked to derive a second form of the equations maintaining full nonlinear rotations. However, these equations turn out to be exactly the same as the HH SWEs (Huang & Hsiung 1996), and a detailed alternative derivation of the HH SWEs is given in Alemi Ardakani & Bridges (2009*d*).

11. Numerical algorithm for shallow-water sloshing

The numerical method we propose for simulation of shallow-water sloshing in a vehicle undergoing rigid-body motion is an extension of the numerical scheme in Alemi Ardakani & Bridges (2009*a*). It is a finite-difference scheme, using centered differencing in space. It is fully implicit and has a block-tridiagonal structure. The basic formulation of the algorithm was first proposed by Leendertse (1967) and refined by Abbott and Ionescu, and is widely used in computational hydraulics (cf. Abbott 1979). The only new features in the algorithm are extension to include a fully 3-D rotation and translation field, and exact implementation of boundary conditions. The fact that the scheme is implicit makes the introduction of rotations straightforward. Some explicit schemes are unstable in the presence of rotation.

The 1-D version of the algorithm was used in Alemi Ardakani & Bridges (2009*a*) and the 2-D version is just a concatenation of this scheme: the time step is split into two steps and an alternating direction implicit algorithm is used: implicit in the x-direction and explicit in the y-direction in the first half step and explicit in the x-direction and implicit in the y-direction in the second half step. One of the nice properties of the scheme is that the boundary conditions at the walls are implemented exactly, even at the intermediate time steps.

The scheme has numerical dissipation, but the form of the dissipation is similar to the action of viscosity. The truncation error is of the form of the heat equation, and so is strongly wavenumber-dependent. Moreover, the numerical dissipation closely follows the hydraulic structure of the equations. See the technical report of Alemi Ardakani & Bridges (2009*e*) for an analysis of the form of the numerical dissipation. The numerical dissipation is helpful for eliminating transients and spurious high-wavenumber oscillation in the formation of travelling hydraulic jumps.

In contrast, Pantazopoulos (1987, 1988) use Glimm's method, which is very effective for treating a large number of travelling hydraulic jumps, but the solutions are discontinuous, and the scheme has problems with mass conservation. Huang & Hsiung (1996, 1997) use flux–vector splitting. This method involves computing eigenvalues of the Jacobian matrices, and is effective for tracking multi-directional characteristics. It appears to be very effective and accurate but is more complicated to implement than the scheme proposed here.

Setting up the equations for the scheme proposed here is straightforward and follows the 1-D construction in Alemi Ardakani & Bridges (2009*a*), but the details are lengthy. Hence, we have given a detailed construction of the algorithm in an internal report (Alemi Ardakani & Bridges 2009*e*) and, in Appendix D, just the main features are highlighted.

12. Sloshing with roll–pitch and roll–pitch–yaw forcing of the vessel

In this section, the forcing is represented using Euler angles. The exact representations for roll–pitch and roll–pitch–yaw used in the simulations are recorded in Appendix C.

12.1. *Sloshing due to roll–pitch forcing*

Roll–pitch forcing is the simplest rotation which is fully 3-D and non-commutative. With a harmonic representation of the angles, it is a simple model for the motion of a rolling and pitching ship. There are results in the literature on roll–pitch forcing of a vessel containing shallow-water fluid (e.g. Dillingham & Falzarano 1986; Falzarano *et al.* 2002), but in all cases, the forcing is linearized so that the angular velocity is the

derivative of an angle. As far as we are aware, the results presented here are the first to use an exact 3-D representation of the roll–pitch motion in the simulations. Three simulations are presented: near resonance, far from resonance, both with quiescent initial conditions and then a roll–pitch simulation where vorticity has been injected into the initial condition.

The angles are taken to be harmonic:

$$\phi(t) = \varepsilon_r \sin(\omega_r t) \quad \text{and} \quad \theta(t) = \varepsilon_p \sin(\omega_p t). \tag{12.1}$$

The body representation of the angular velocity is

$$\boldsymbol{\Omega}(t) = \begin{pmatrix} \varepsilon_r \omega_r \cos(\omega_r t) \cos(\varepsilon_p \sin \omega_p t) \\ \omega_p \varepsilon_p \cos \omega_p t \\ \varepsilon_r \omega_r \cos(\omega_r t) \sin(\varepsilon_p \sin \omega_p t) \end{pmatrix}, \tag{12.2}$$

and the gravity vector is

$$\boldsymbol{g}(t) := g \boldsymbol{Q}^{\mathrm{T}} \boldsymbol{e}_3 = g \begin{pmatrix} -\cos\phi(t)\ \sin\theta(t) \\ \sin\phi(t) \\ \cos\phi(t)\ \cos\theta(t) \end{pmatrix}. \tag{12.3}$$

The vessel and fluid geometry parameters are set at

$$\left.\begin{array}{lll} L_1 = 1.0\,\mathrm{m}, & L_2 = 0.80\,\mathrm{m}, & h_0 = 0.12\,\mathrm{m}, \\ d_1 = -0.50\,\mathrm{m}, & d_2 = -0.40\,\mathrm{m}, & d_3 = 0.0\,\mathrm{m}. \end{array}\right\} \tag{12.4}$$

With this fluid geometry, the natural frequencies (9.13) are

$$\omega_{mn} \approx 3.40 \left(m^2 + \frac{n^2}{0.64} \right)^{1/2} \ \mathrm{rad\,s^{-1}}, \tag{12.5}$$

with the first two: $\omega_{10} \approx 3.41\,\mathrm{rad\,s^{-1}}$ and $\omega_{01} \approx 4.26\,\mathrm{rad\,s^{-1}}$.

In shallow-water sloshing in one horizontal space dimension, a travelling hydraulic jump forms when the vessel is forced harmonically near resonance. Here we see a similar phenomenon, although the multi-component forcing generates a hydraulic jump with a curved wavefront. Figure 3 shows the generation of the bore after only 2 s of real time. In the figures, the X–Y–Z coordinate system is the fixed inertial frame, and the actual position of the tank relative to that frame is plotted. The numerical parameters in this case are $\Delta x = 0.02$, $\Delta y = 0.016$ and $\Delta t = 0.01$, and the initial conditions are quiescent: $h(x, y, 0) = h_0$ and $u(x, y, 0) = v(x, y, 0) = 0$.

Now suppose that the forcing frequencies are far from resonance. The vessel and fluid geometry parameters are set at

$$\left.\begin{array}{lll} L_1 = 1.0\,\mathrm{m}, & L_2 = \frac{1}{2}L_1 = 0.5\,\mathrm{m}, & h_0 = 0.12\,\mathrm{m}, \\ d_1 = -0.5\,\mathrm{m}, & d_2 = -0.25\,\mathrm{m}, & d_3 = 0.0\,\mathrm{m}. \end{array}\right\} \tag{12.6}$$

The first two natural frequencies of the fluid are $\omega_{10} \approx 3.4085$ and $\omega_{01} \approx 6.8171$. Figure 4 shows snapshots of the free surface at a sequence of times. Even with the much larger forcing amplitude, the motion of the free surface is quite gentle for long times. The initial conditions are quiescent and the numerical parameters are $\Delta x = 0.02$, $\Delta y = 0.01$ and $\Delta t = 0.01$.

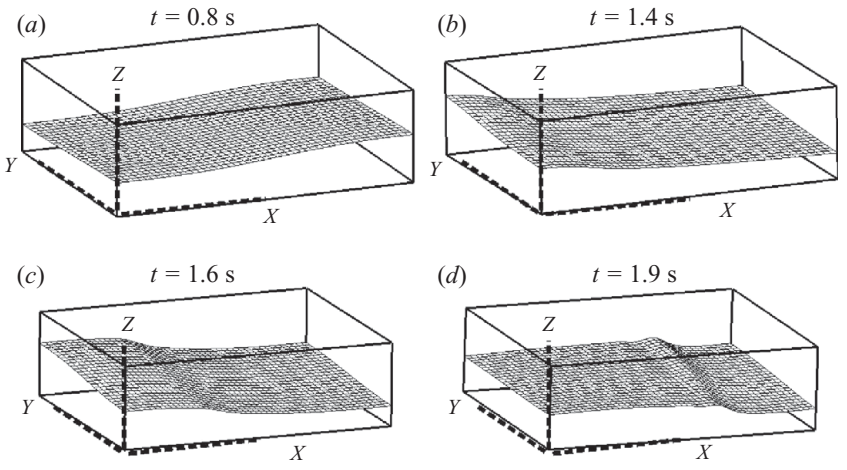

FIGURE 3. Snapshots showing the emergence of a curved hydraulic jump when the forcing parameters are $\varepsilon_p = 2.0°$, $\varepsilon_r = 1.0°$, $\omega_p = 4.2607$ and $\omega_r = 3.4085$ rad s^{-1}.

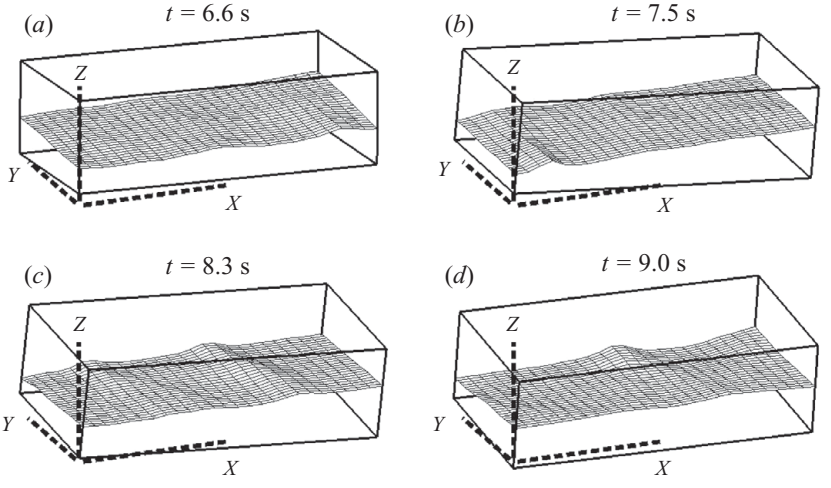

FIGURE 4. Snapshots of free-surface profile for coupled roll–pitch forcing, far from resonance, with $\varepsilon_p = 5.0°$, $\varepsilon_r = 7.0°$, $\omega_p = 1.0225$ rad s^{-1} and $\omega_r = 0.8521$ rad s^{-1}.

12.2. *Roll–pitch forcing with vorticity injected into the initial condition*

Vorticity can be injected into the initial condition. Consider the following form, and take $h(x, y, 0) = h_0$ but with a non-trivial velocity field:

$$\left.\begin{aligned} U(x, y, 0) &= A \sin\left(\frac{m\pi x}{L_1}\right) \cos\left(\frac{n\pi y}{L_2}\right), \\ V(x, y, 0) &= -\frac{m}{n}\frac{L_2}{L_1} A \cos\left(\frac{m\pi x}{L_1}\right) \sin\left(\frac{n\pi y}{L_2}\right), \end{aligned}\right\} \tag{12.7}$$

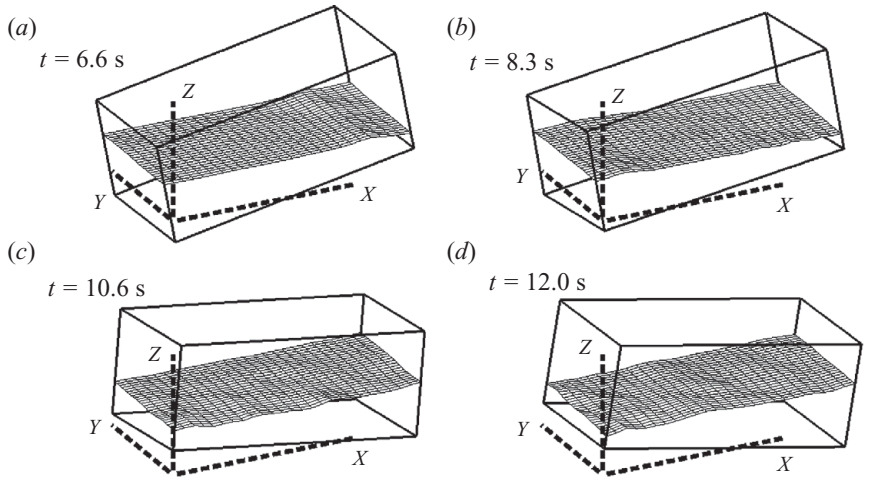

FIGURE 5. Configuration of the free-surface profile for large-amplitude roll–pitch forcing with vorticity in the initial condition.

where A is an input amplitude, and m, n are arbitrary natural numbers. This velocity field is divergence-free and has vertical vorticity field

$$(V_x - U_y)|_{t=0} = \frac{\pi A L_2}{n}\left(\frac{m^2}{L_1^2} + \frac{n^2}{L_2^2}\right)\sin\left(\frac{m\pi x}{L_1}\right)\sin\left(\frac{n\pi y}{L_2}\right). \tag{12.8}$$

For the simulation, the vessel and fluid geometry parameters are set at

$$\left.\begin{array}{l} L_1 = 0.5\,\mathrm{m}, \quad L_2 = 0.25\,\mathrm{m}, \quad h_0 = 0.08\,\mathrm{m}, \\ d_1 = -0.25\,\mathrm{m}, \quad d_2 = -0.125\,\mathrm{m}, \quad d_3 = 0.0\,\mathrm{m}. \end{array}\right\} \tag{12.9}$$

The vorticity parameters are set at $A = 0.08$, and $m = n = 3$.

The first two natural frequencies of the fluid are $\omega_{10} \approx 5.5662$ and $\omega_{01} \approx 11.1324$. Pitch and roll motions are taken to be harmonic and the same form as (12.1) with parameters

$$\varepsilon_p = 10.87^\circ, \quad \varepsilon_r = 7.1^\circ, \quad \omega_p = 0.6679\ \mathrm{rad\,s^{-1}}, \quad \omega_r = 0.5010\ \mathrm{rad\,s^{-1}}. \tag{12.10}$$

Figure 5 shows the configuration of the free surface at a sequence of times. Although the amplitude is quite large, the motion of the free surface remains quite gentle. It appears that the vorticity enhances the mixing of the interior fluid, but does not greatly affect the free surface. The numerical parameters in this simulation are $\Delta x = 0.01$, $\Delta y = 0.005$ and $\Delta t = 0.01$.

12.3. *Forcing using exact Euler-angle representation of pitch–roll–yaw*

The only results in the literature where full roll–pitch–yaw forcing of sloshing is reported is in Huang & Hsiung (1996). (See also Huang (1995) and Huang & Hsiung (1997).). However, although their formulation includes this forcing, their results are limited to planar rotations. Hence, the results reported here are the first sloshing simulations with full roll–pitch–yaw forcing.

The 3–2–1 Euler angles are used and the properties needed are recorded in § C.1. The expression for $\boldsymbol{Q}$ is given in (C 4) and the required body representation of the angular velocity is given in (C 5). The yaw, pitch and roll angles are taken to be

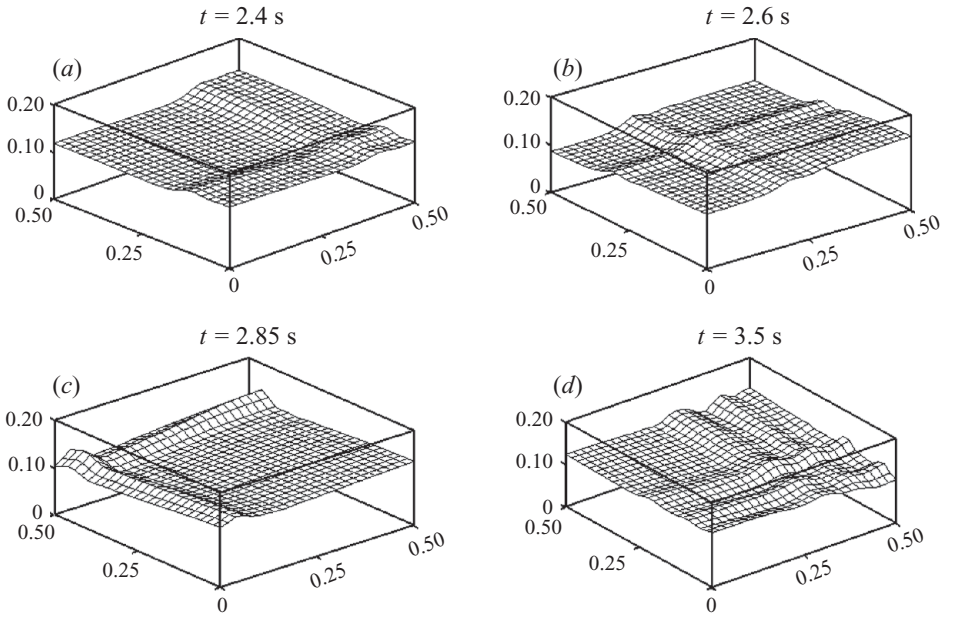

FIGURE 6. Snapshots of surface profile due to roll, pitch and yaw with forcing (12.11).

harmonic:

$$\psi(t) = \varepsilon_y \sin(\omega_y t), \quad \theta(t) = \varepsilon_p \sin(\omega_p t), \quad \phi(t) = \varepsilon_r \sin(\omega_r t). \tag{12.11}$$

The gravity vector is

$$\boldsymbol{g}(t) := g\mathbf{Q}^{\mathrm{T}}\boldsymbol{e}_3 = g\begin{pmatrix} -\sin\theta(t) \\ \sin\phi(t)\cos\theta(t) \\ \cos\phi(t)\cos\theta(t) \end{pmatrix}. \tag{12.12}$$

The fluid and vessel geometry parameters are set at

$$\left.\begin{array}{lll} L_1 = 0.50\,\mathrm{m}, & L_2 = 0.50\,\mathrm{m}, & h_0 = 0.12\,\mathrm{m}, \\ d_1 = -0.25\,\mathrm{m}, & d_2 = -0.25\,\mathrm{m}, & d_3 = 0.0\,\mathrm{m}. \end{array}\right\} \tag{12.13}$$

With this geometry, the natural frequencies are

$$\omega_{mn} \approx 6.82\sqrt{m^2+n^2}\ \mathrm{rad\,s^{-1}}. \tag{12.14}$$

We will present results for a typical run in this configuration. Take the forcing function parameters to be

$$\varepsilon_y = 2.0^\circ, \quad \varepsilon_p = 1.0^\circ, \quad \varepsilon_r = 1.0^\circ, \quad \omega_y = \omega_p = \omega_r = 5.2171\ \mathrm{rad\,s^{-1}}, \tag{12.15}$$

and set the numerical parameters at $\Delta x = \Delta y = 0.01$ and $\Delta t = 0.01$. With this low amplitude of forcing, the singularity of the Euler angles is safely avoided.

Snapshots of the surface profile at a sequence of times are depicted in figure 6. Almost immediately a pair of interacting travelling waves, close to a bore, are generated. They are very similar to the standing cnoidal waves that can be found analytically (e.g. Bridges 1987). However, the waves here do not maintain form after many interactions.

12.4. *Discussion*

We have just scratched the surface of possibilities in the study of the implications of 3-D rotations on sloshing. As expected, near-resonant forcing produces travelling hydraulic jumps, and far from resonant forcing produces gentle sloshing.

However, the situation here is much more complicated than the case of one horizontal space dimension, since there are two frequencies in roll–pitch and three frequencies in roll–pitch–yaw. In one horizontal space dimension, the theory is very clear: there is a region in frequency space about resonance, where the response is a travelling hydraulic jump (e.g. Ockendon & Ockendon 1973; Kobine 2008). In two horizontal space dimensions, there is more than one frequency, and more types of hydraulic jump, and the hydraulic jumps have wavefront curvature, and can interact.

Another feature that arises here is the interaction between the multiple forcing functions. For example, there are dynamical systems implications when the ratio of ω_p to ω_r is irrational. In this case, the forcing is quasi-periodic rather than periodic. In the dynamical systems literature, Wiggins (1987) shows that a Duffing oscillator with quasi-periodic forcing can have a chaotic response. In the context of sloshing, there is the additional potential for chaotic interaction between travelling hydraulic jumps. Furthermore, there are implications for the generation of PV.

In the above simulations, the typical number of grid points in space is about 2500. CPU time is about 5 s per time step without any special optimization: coded in MATLAB and run on a 32 bit 2.0 GHz processor. The simulations are run for 500–600 time steps. Typically, two to three iterations are required per time step, and when hydraulic jumps are present, the number of iterations is increased to 5–7 per time step.

13. Sloshing in vessels undergoing pure yaw motion

The case of pure yaw forcing is of interest for several reasons. Firstly, there is a simplified form of PV conservation; secondly, the surface SWEs and the HH SWEs agree in this case (assuming equal velocity fields) and so the results can be compared, and thirdly, this case is the closest to the rotating SWEs in geophysical fluid dynamics.

In the case of pure yaw forcing, the coefficients in the surface SWEs reduce considerably. With $\Omega_1 = \Omega_2 = 0$ and $\Omega_3 = \dot{\psi}$, where $\psi(t)$ is the yaw angle,

$$\left.\begin{aligned} a_{11} &= a_{22} = g, \quad a_{12} = a_{21} = 0, \\ b_1 &= 2\Omega_3 V + \Omega_3^2(x + d_1) + \dot{\Omega}_3(y + d_2), \\ b_2 &= -2\Omega_3 U + \Omega_3^2(y + d_2) - \dot{\Omega}_3(x + d_1). \end{aligned}\right\} \tag{13.1}$$

The surface equations and the HH equations are identical (assuming equivalent velocity fields) and the momentum equations reduce to the classical SWEs with forcing

$$\left.\begin{aligned} U_t + UU_x + VU_y + gh_x &= 2\dot{\psi}V + \dot{\psi}^2(x + d_1) + \ddot{\psi}(y + d_2), \\ V_t + UV_x + VV_y + gh_y &= -2\dot{\psi}U + \dot{\psi}^2(y + d_2) - \ddot{\psi}(x + d_1). \end{aligned}\right\} \tag{13.2}$$

The general expression for PV in § 8 reduces in this case to

$$\mathsf{PV} := \frac{V_x - U_y + 2\dot{\psi}}{h}. \tag{13.3}$$

Consider the yaw motion to be harmonic:

$$\psi(t) = \varepsilon_y \sin(\omega_y t) \quad \text{with} \quad \varepsilon_y = 10.0^\circ, \quad \text{and} \quad \omega_y = 4.1746 \text{ rad s}^{-1}. \tag{13.4}$$

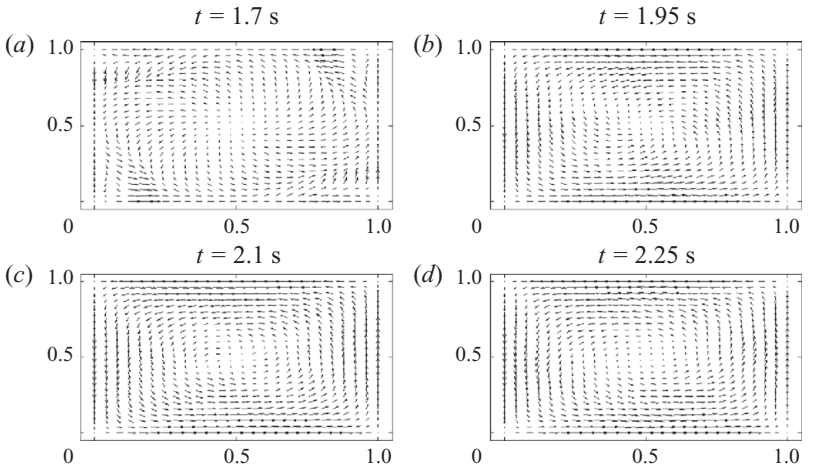

FIGURE 7. Velocity fields associated with the pure yaw forcing (see (13.4)).

Set the vessel and fluid parameters at

$$\left.\begin{array}{l} L_1 = 1.0\,\mathrm{m}, \quad L_2 = 1.0\,\mathrm{m}, \quad h_0 = 0.18\,\mathrm{m}, \\ d_1 = -0.5\,\mathrm{m}, \quad d_2 = -0.5\,\mathrm{m}, \quad d_3 = -0.3\,\mathrm{m}. \end{array}\right\} \tag{13.5}$$

The forcing frequency is near the lowest natural frequency. The natural frequencies are

$$\omega_{mn} \approx 4.1746\sqrt{m^2+n^2}\ \mathrm{rad\,s^{-1}}. \tag{13.6}$$

The numerical parameters are set at $\Delta x = \Delta y = 0.02$ and $\Delta t = 0.01$.

The field of velocity vectors is shown at different values of time in figure 7. There is a very clear swirling motion set-up. The conservation of PV generates a vertical vorticity field, and this is evident in the figures.

13.1. *Comparison with results of Huang & Hsiung (1996)*

Now change the parameters in order to compare with the results of Huang & Hsiung (1996). Set the vessel and fluid parameters at

$$\left.\begin{array}{l} L_1 = 1.0\,\mathrm{m}, \quad L_2 = 0.8\,\mathrm{m}, \quad h_0 = 0.1\,\mathrm{m}, \\ d_1 = -0.5\,\mathrm{m}, \quad d_2 = -0.4\,\mathrm{m}, \quad d_3 = 0.0\,\mathrm{m}. \end{array}\right\} \tag{13.7}$$

The numerical parameters are

$$\Delta x = 0.02\,\mathrm{m}, \quad \Delta y = 0.016\,\mathrm{m}, \quad \Delta t = 0.01\,\mathrm{s}. \tag{13.8}$$

The forcing is harmonic yaw motion as in (13.4) with parameters

$$\varepsilon_y = 4.0^\circ, \quad \omega_y = 6.0\ \mathrm{rad\,s^{-1}}. \tag{13.9}$$

The snapshot of the surface profile at $t = 1.5$ s and the corresponding velocity field are depicted in figure 8. This result agrees very well with figures 28 and 29 of Huang & Hsiung (1996), including the vortex pattern. The initial conditions are vorticity-free. Hence, the generation of vorticity is due to the imposed rotation, but it appears to be enhanced by the numerical dissipation-like truncation error.

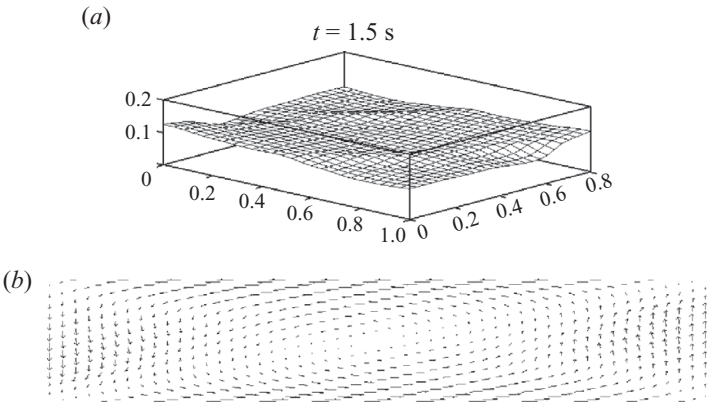

FIGURE 8. Surface profile and velocity field due to yaw at $t = 1.5$ s: comparison of the numerics based on the surface SWEs with figures 28 and 29 of Huang & Hsiung (1996).

14. Diagonal and swirling waves due to coupled surge–sway motion

Surge–sway forcing is the most studied of forcing functions for 3-D sloshing (e.g. Wu *et al.* 1998; Faltinsen *et al.* 2003; Liu & Lin 2008; Chen *et al.* 2009; Wu & Chen 2009). It is simple to implement since there is only translation and no orientation change. On the other hand, there are identifiable wave types and bifurcations that occur that make it easier for experimental and theoretical comparison. The results in this section are inspired by the theory and experiment of Faltinsen *et al.* (2003) and the 3-D simulations of Wu & Chen (2009). The purpose is to show that the shallow-water model captures the essential features of diagonal and swirling waves.

To capture diagonal modes, the prescribed surge and sway motions of the vessel are taken to be harmonic and in phase:

$$q_1(t) = \varepsilon_1 \cos(\omega_1 t) \quad \text{and} \quad q_2(t) = \varepsilon_2 \cos(\omega_2 t). \tag{14.1}$$

Set the fluid and vessel geometry parameters at

$$L_1 = 0.5\,\text{m}, \quad L_2 = 0.5\,\text{m} \quad \text{and} \quad h_0 = 0.07\,\text{m}, \tag{14.2}$$

giving a fluid aspect ratio of $h_0/L_1 = 0.14$, and natural frequencies

$$\omega_{mn} \approx 5.207\sqrt{m^2 + n^2}\ \text{rad}\,\text{s}^{-1}. \tag{14.3}$$

The numerical parameters are taken to be $\Delta x = \Delta y = 0.025$ m and $\Delta t = 0.01$ s.

Following the strategy in the experiments of Faltinsen *et al.* (2003) and the simulations of Wu & Chen (2009), points on the vessel walls are identified and the time series at the fixed points are compared. We will restrict attention to two points on the vessel walls which we identify as P_6 and P_7 (see figure 13*b* in Faltinsen *et al.* 2003). Their locations are

$$P_6 : (x, y) = \left(L_1, \tfrac{1}{2}L_2\right), \quad P_7 : (x, y) = \left(\tfrac{1}{2}L_1, 0\right). \tag{14.4}$$

((P_6, P_7) here correspond to (P_1, P_6) in Faltinsen *et al.* (2003).)

14.1. *Surge–sway motion with diagonal forcing*

The forcing function parameters for diagonal forcing with forcing frequency well above the lowest natural frequency are

$$\varepsilon_1 = 0.002\,\text{m}, \quad \varepsilon_2 = 0.002\,\text{m} \quad \text{and} \quad \omega_1 = \omega_2 = 1.4\,\omega_{1,0} = 7.2893\,\text{rad}\,\text{s}^{-1}. \tag{14.5}$$

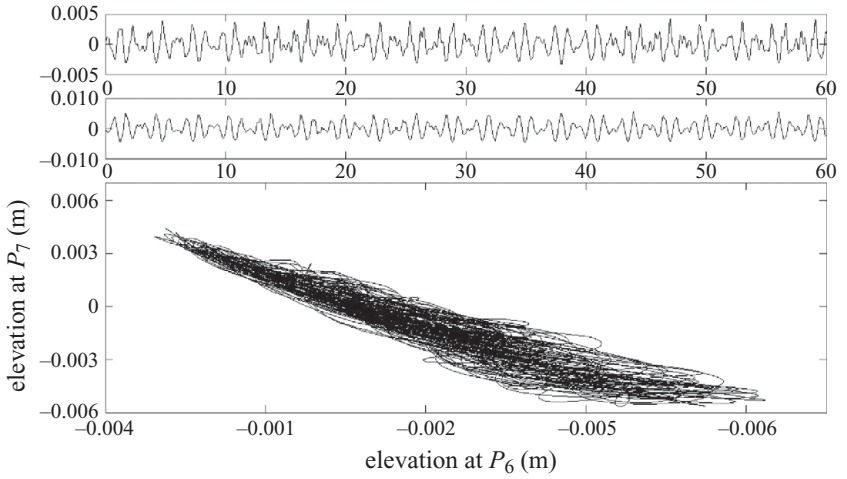

FIGURE 9. Time histories of the surface displacements at points P_6 and P_7, and a parametric graph of the pair (P_6,P_7).

The time histories of the surface displacement at points P_6 and P_7 and the parametric curve of the pair are shown in figure 9. The parametric graph in figure 9 has a non-trivial slope. According to the theory of Faltinsen *et al.* (2003), this type of parametric graph indicates square-like waves in the tank. A square-like wave corresponds to a nearly diagonal standing wave. (See the last few sentences of p. 17 of Faltinsen *et al.* (2003).) The structure of a square-like wave is also seen in figures 7(*b*), 8(*b*) and 9(*b*) of Wu & Chen (2009).

14.2. *Surge–sway forcing with a phase shift*

By taking the surge and sway forcing functions to be out of phase, a clear example of a swirling wave emerges. Consider the case of diagonal forcing with the surge and sway 90° out of phase:

$$q_1(t) = \varepsilon_1 \cos(\omega_1 t) \quad \text{and} \quad q_2(t) = \varepsilon_2 \sin(\omega_2 t). \tag{14.6}$$

The parameters (14.2) and the numerical parameters remain the same, and the forcing function parameters are taken to be

$$\varepsilon_1 = 0.00012\,\text{m}, \quad \varepsilon_2 = 0.00012\,\text{m} \quad \text{and} \quad \omega_1 = \omega_2 = 0.99\omega_{1,0} = 5.1546\,\text{rad}\,\text{s}^{-1}. \tag{14.7}$$

The time histories of the surface displacement at points P_6 and P_7, and their parametric curve are shown in figures 10 and 11, respectively. Figure 12 shows surface plots at a sequence of times which very clearly show the propagation of a counterclockwise swirling wave. These surface plots agree qualitatively with the surface plots of a swirling wave in figure 11 of Wu & Chen (2009).

Additional contour plots and simulations of surge–sway are given in the report of Alemi Ardakani & Bridges (2009*f*).

15. Sloshing on the London Eye

The London Eye is a large ferris wheel on the edge of the Thames River in London. A schematic of the attached vessel on the London Eye is shown in figure 13. Mathematically, the vessel, partially filled with fluid, is prescribed to travel along a

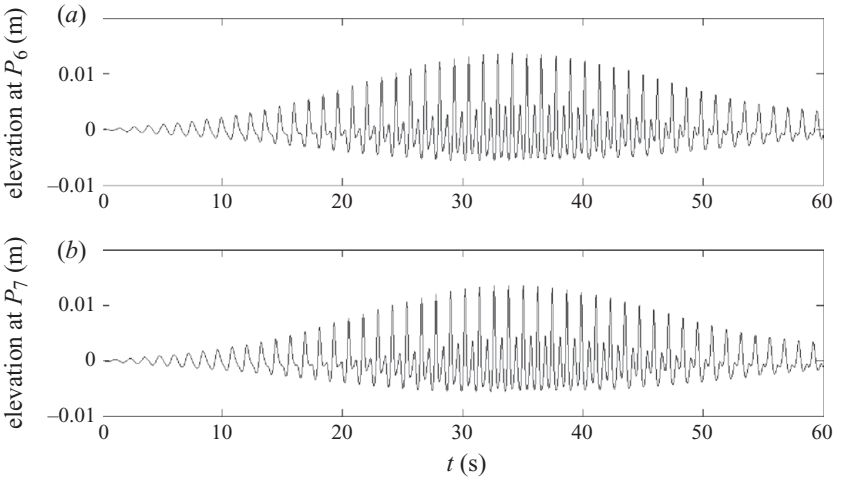

FIGURE 10. Time histories of surface displacements at points P_6 and P_7 associated with the out-of-phase forcing (14.7).

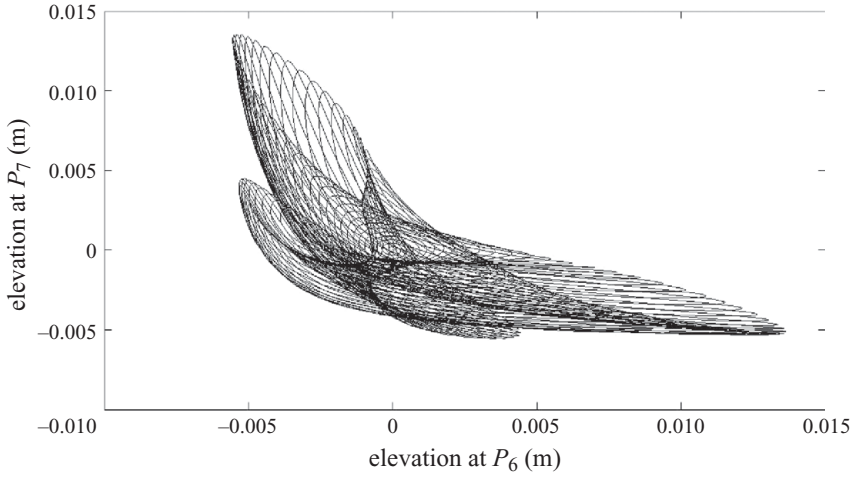

FIGURE 11. Parametric graph of the pair (P_6,P_7) associated with the out-of-phase forcing (see (14.7)).

circular path. Even when the speed along the path is constant, sloshing occurs due to change in the direction. The base of the vessel remains horizontal along the path. In addition, the vessel can also have a prescribed rotation.

The interest in this example is threefold. It is an example with very large displacements of the vehicle and illustrates the generality of the prescribed vessel motion. Secondly, it is a prototype for the transport of a vessel along a surface. In this case, the surface is a great circle on the two-sphere. As the vehicle moves along the surface, it can also rotate relative to the point of attachment. Other examples of surfaces of interest are the full two-sphere or a bumpy sphere, which is a model for a satellite containing fluid and orbiting the earth, and a surface modelling terrain. The latter is a model for vehicles transporting liquid on roads through hilly terrain.

Thirdly, it is an excellent setting to test control strategies for sloshing. For example, suppose the speed along a path in the surface is prescribed. Sloshing will result if the

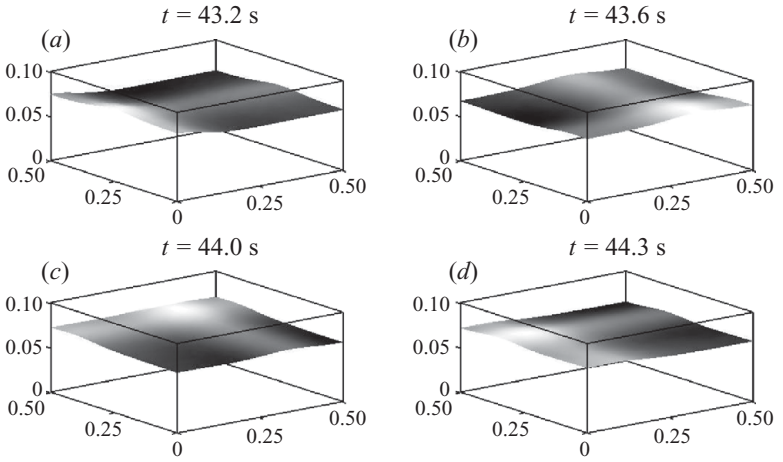

FIGURE 12. Surface plots of surface profile at different times associated with the out-of-phase forcing (see (14.7)).

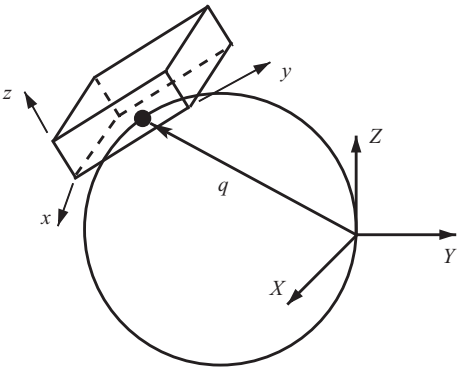

FIGURE 13. Schematic showing an attached vessel which moves along a circular path, modelling a pod on the London Eye.

path is curved due to induced acceleration. The local rotation of the body could act as a control, and roll, pitch or yaw could be induced to counteract any sloshing due to motion along the path.

In this section, the basic model is introduced, and a simulation of the vessel moving along the circle at constant speed, with coupled roll–pitch motion, is presented. The interest in this example is as a prototype for more general trajectories, since the actual London Eye is designed to have extremely low centripetal acceleration. According to the London Eye website, the radius, R, of the wheel is 65 m, and the travel time of a pod is 30 min, giving a frequency of $\omega_c = \pi/900$. The relevant dimensionless parameter is the ratio of centripetal acceleration to gravity:

$$Fr^2 = \frac{\omega_c^2 R}{g}. \tag{15.1}$$

This parameter is like a Froude number (p. 111 of Vanyo 1993), since the ratio is a velocity squared over gR, but it is a vessel-motion parameter and not a fluid

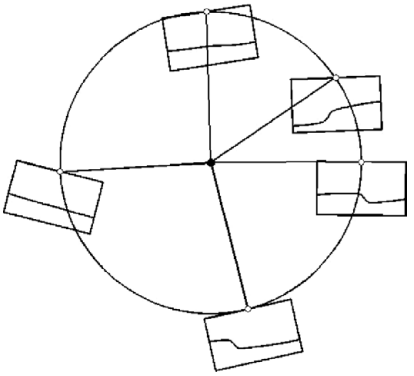

FIGURE 14. Planar example, illustrating the fluid motion as the vessel moves along the circle.

parameter. The Froude number for the London Eye is

$$Fr \approx 0.009. \tag{15.2}$$

This Froude number is quite low (passengers can disembark from the London Eye without it changing speed), and so we will increase it by an order of magnitude in order to induce sloshing fluid motion.

The radius of the circle is denoted by R. The vector $\boldsymbol{q}(t) = (q_1(t), q_2(t), q_3(t))$ defines the distance from the origin of the fixed coordinate system to the point of attachment of the vessel on the circle,

$$q_1(t) = 0, \quad q_2(t) = -R + R\,\cos\theta_c(t) \quad \text{and} \quad q_3(t) = R\,\sin\theta_c(t), \quad \text{with} \quad \theta_c(t) = \omega_c t. \tag{15.3}$$

Here ω_c is the angular speed along the path and it is taken to be a specified constant.

An example of purely plane motion, where the vehicle moves along the curve at constant speed, and has an added harmonic pitch forcing about the suspension point, is shown in figure 14. In this case, the axis of rotation is above the still-water level and the vessel is suspended. In the planar case, we have made videos of the coupled motion and these are very effective at illustrating the coupled slosh–vehicle dynamics, and they are available at http://personal.maths.surrey.ac.uk/st/T.Bridges/SLOSH/.

For the 3-D case, the point of attachment of the vessel will be allowed to undergo a prescribed 3-D rotation. For definiteness, take this rotation to be of the roll–pitch form, as defined in Appendix C and §12. The pitch and roll motions are taken to be harmonic and of the same form as (12.1). The initial conditions are taken to be quiescent.

The vessel and fluid geometry parameters are set at

$$\left.\begin{array}{lll} L_1 = 1.0\,\text{m}, & L_2 = 0.80\,\text{m}, & h_0 = 0.15\,\text{m}, \\ d_1 = -0.5\,\text{m}, & d_2 = -0.4\,\text{m}, & d_3 = 0.0\,\text{m}. \end{array}\right\} \tag{15.4}$$

The geometric parameters associated with the path are set at $R = 1.2\,\text{m}$ and $\omega_c = 0.4\ \text{rad}\,\text{s}^{-1}$.

For this vessel motion, the assumption (7.7), in the form (7.13), arises, and it can be formulated in terms of the Froude number (15.1). The condition (7.13) is equivalent to assuming that Fr is small compared to unity. For the above parameter values,

$$Fr \approx 0.14, \tag{15.5}$$

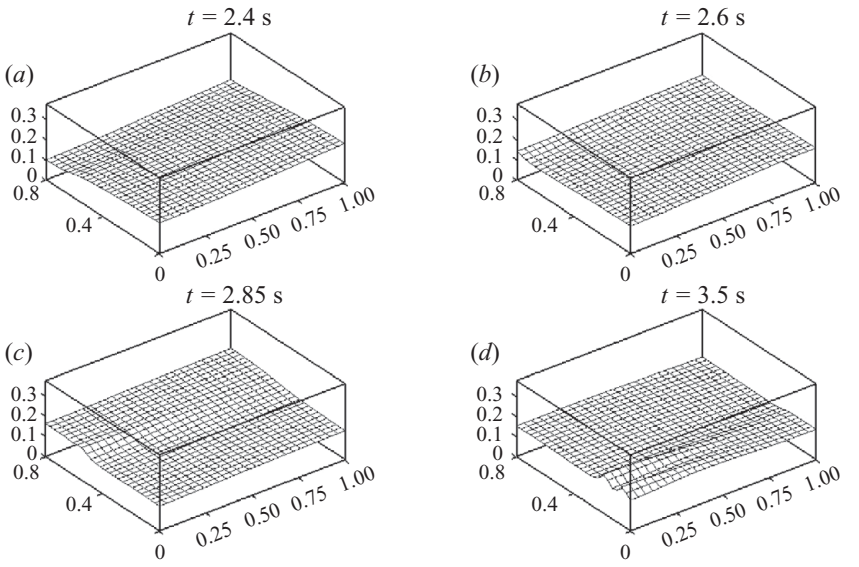

FIGURE 15. Snapshots of free-surface profile for roll–pitch forcing along the path modelling the London Eye example: the angle θ_c goes from 55 to 80° in the sequence.

and so the condition (7.13) is well satisfied, but it is still an order of magnitude larger than that of the London Eye. The numerical parameters are set at $\Delta x = 0.02$, $\Delta y = 0.016$ and $\Delta t = 0.01$. The first two natural frequencies of the fluid are $\omega_{10} \approx 3.81$ and $\omega_{01} \approx 4.76$.

Figures 15 and 16 show snapshots of the free surface at a sequence of times when

$$\varepsilon_p = 1.0^\circ, \quad \varepsilon_r = 1.0^\circ, \quad \omega_p = 0.2\omega_{01} \approx 0.9527\,\mathrm{rad\,s^{-1}}, \quad \omega_r = 0.95\omega_{10} \approx 3.6204\,\mathrm{rad\,s^{-1}}. \tag{15.6}$$

Two prominent features show up. Firstly, there is a bias towards one side of the tank due to the induced accelerations from the path. Secondly, even though the second frequency is near the resonant frequency, the response is relatively gentle, indicative of the interaction between the $\boldsymbol{q}(t)$ path forcing and the roll–pitch forcing.

16. Concluding remarks

A new set of SWEs which model the 3-D rigid-body motion of a vessel containing fluid has been derived. The only assumptions are on the vertical velocity and acceleration at the surface. The equations give new insight into shallow-water sloshing, and numerical simulations include the effect of viscosity and are much faster than the full 3-D equations. It has been demonstrated that the equations capture many of the features of 3-D sloshing for the case when the free surface is single-valued: diagonal waves, swirling waves, curved hydraulic jumps and interacting waves. A form of vorticity is captured by the equations and numerics, and the motion of the vessel can be specified in complete generality.

In this paper, the vessel motion has been prescribed. The vessel motion can also be determined by solving the rigid-body equations coupled to the fluid motion. Some results, for the case of coupled motion for a rigid body with shallow-water fluid in two dimensions, have been obtained recently (**?**Alemi Ardakani & Bridges 2010). The extension to coupling between 3-D rigid-body motion and shallow-water sloshing is,

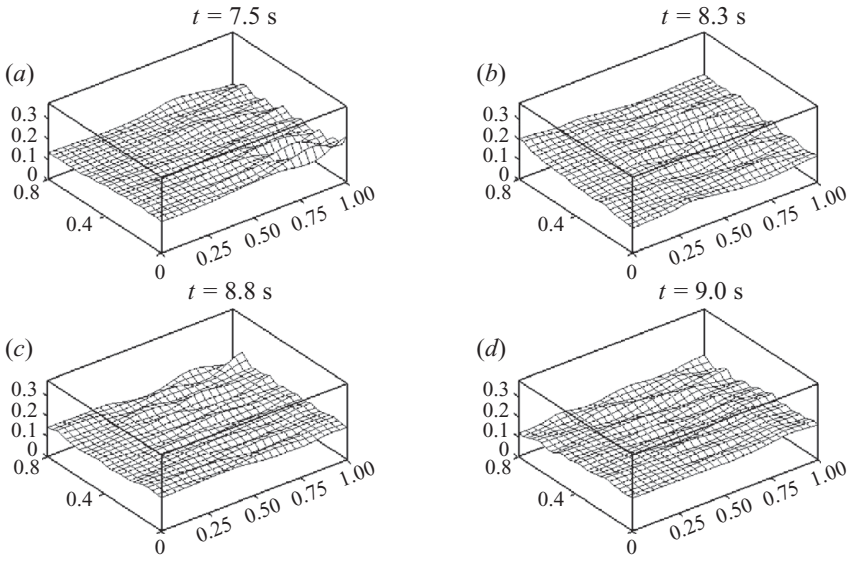

FIGURE 16. Snapshots of free-surface profile for roll–pitch forcing along the path modelling the London Eye example: the angle θ_c goes from 172 to 206° in the sequence.

however, a big step due to the nature of rotations in three dimensions. The equations of 3-D rigid-body motion coupled to sloshing have been derived by Veldman *et al.* (2007) for the case of sloshing in spacecraft. However, simulation in this case is very time-consuming. The new surface SWEs introduced here represent the vehicle motion exactly, and therefore, provide an opportunity for efficient simulation of the coupling between the vehicle motion and 3-D shallow-water sloshing.

Appendix A. The horizontal pressure gradient

A.1. *x-Derivative of pressure*

Differentiate (3.4) with respect to x:

$$\frac{1}{\rho}\frac{\partial p}{\partial x} = h_x \frac{\mathrm{D}w}{\mathrm{D}t}\bigg|^h + \int_z^h \left(\frac{\mathrm{D}w}{\mathrm{D}t}\right)_x \mathrm{d}s + 2\Omega_1 V h_x + 2\Omega_1 \int_z^h v_x \,\mathrm{d}s - 2\Omega_2 U h_x$$
$$- 2\Omega_2 \int_z^h u_x \,\mathrm{d}s - \left(\Omega_1^2 + \Omega_2^2\right)(h + d_3)h_x - \beta_x(h - z) - \beta h_x - \sigma\,\partial_x \mathrm{div}(\boldsymbol{\kappa}). \quad \text{(A 1)}$$

Use the vorticity equation to substitute for $(\mathrm{D}w/\mathrm{D}t)_x$, we get

$$\frac{1}{\rho}\frac{\partial p}{\partial x} = h_x \frac{\mathrm{D}w}{\mathrm{D}t}\bigg|^h + \int_z^h \left[\left(\frac{\mathrm{D}u}{\mathrm{D}t}\right)_z - 2\Omega_1 \frac{\partial v}{\partial x} - 2\Omega_2 \frac{\partial v}{\partial y} - 2\Omega_3 \frac{\partial v}{\partial z} + 2\dot{\Omega}_2\right] \mathrm{d}s$$
$$+ 2\Omega_1 V h_x + 2\Omega_1 \int_z^h v_x \,\mathrm{d}s - 2\Omega_2 U h_x - 2\Omega_2 \int_z^h u_x \,\mathrm{d}s$$
$$- \left(\Omega_1^2 + \Omega_2^2\right)(h + d_3)h_x - \beta_x(h - z) - \beta h_x - \sigma\,\partial_x \mathrm{div}(\boldsymbol{\kappa}), \quad \text{(A 2)}$$

or

$$\frac{1}{\rho}\frac{\partial p}{\partial x} = h_x \frac{\mathrm{D}w}{\mathrm{D}t}\bigg|^h + \frac{\mathrm{D}u}{\mathrm{D}t}\bigg|_z^h - 2\Omega_1 \int_z^h v_x \,\mathrm{d}s - 2\Omega_2 \int_z^h v_y \,\mathrm{d}s - 2\Omega_3 \int_z^h v_z \,\mathrm{d}s + 2\dot{\Omega}_2(h-z)$$
$$+ 2\Omega_1 V h_x + 2\Omega_1 \int_z^h v_x \,\mathrm{d}s - 2\Omega_2 U h_x - 2\Omega_2 \int_z^h u_x \,\mathrm{d}s$$
$$- \left(\Omega_1^2 + \Omega_2^2\right)(h+d_3)h_x - \beta_x(h-z) - \beta h_x - \sigma \partial_x \mathrm{div}(\boldsymbol{\kappa}), \tag{A 3}$$

or

$$\frac{\mathrm{D}u}{\mathrm{D}t} + \frac{1}{\rho}\frac{\partial p}{\partial x} = \frac{\mathrm{D}u}{\mathrm{D}t}\bigg|^h + \frac{\mathrm{D}w}{\mathrm{D}t}\bigg|^h h_x + 2\Omega_2 W - 2\Omega_3 V + 2\dot{\Omega}_2(h-z)$$
$$+ 2\Omega_1 V h_x - 2\Omega_2 U h_x - 2\Omega_2 w + 2\Omega_3 v$$
$$- \left(\Omega_1^2 + \Omega_2^2\right)(h+d_3)h_x - \beta_x(h-z) - \beta h_x - \sigma \partial_x \mathrm{div}(\boldsymbol{\kappa}), \tag{A 4}$$

which is (3.5) in § 3.

A.2. *y-Derivative of pressure*

Differentiate (3.4) with respect to y:

$$\frac{1}{\rho}\frac{\partial p}{\partial y} = h_y \frac{\mathrm{D}w}{\mathrm{D}t}\bigg|^h + \int_z^h \left(\frac{\mathrm{D}w}{\mathrm{D}t}\right)_y \mathrm{d}s + 2\Omega_1 V h_y + 2\Omega_1 \int_z^h v_y \,\mathrm{d}s - 2\Omega_2 U h_y$$
$$- 2\Omega_2 \int_z^h u_y \,\mathrm{d}s - \left(\Omega_1^2 + \Omega_2^2\right)(h+d_3)h_y - \beta_y(h-z) - \beta h_y - \sigma \partial_y \mathrm{div}(\boldsymbol{\kappa}). \tag{A 5}$$

Use the vorticity equation to substitute for $(\mathrm{D}w/\mathrm{D}t)_y$:

$$\frac{1}{\rho}\frac{\partial p}{\partial y} = h_y \frac{\mathrm{D}w}{\mathrm{D}t}\bigg|^h + \int_z^h \left[\left(\frac{\mathrm{D}v}{\mathrm{D}t}\right)_z + 2\Omega_1 \frac{\partial u}{\partial x} + 2\Omega_2 \frac{\partial u}{\partial y} + 2\Omega_3 \frac{\partial u}{\partial z} - 2\dot{\Omega}_1\right] \mathrm{d}s$$
$$+ 2\Omega_1 V h_y + 2\Omega_1 \int_z^h v_y \,\mathrm{d}s - 2\Omega_2 U h_y - 2\Omega_2 \int_z^h u_y \,\mathrm{d}s$$
$$- \left(\Omega_1^2 + \Omega_2^2\right)(h+d_3)h_y - \beta_y(h-z) - \beta h_y - \sigma \partial_y \mathrm{div}(\boldsymbol{\kappa}), \tag{A 6}$$

or

$$\frac{1}{\rho}\frac{\partial p}{\partial y} = h_y \frac{\mathrm{D}w}{\mathrm{D}t}\bigg|^h + \left(\frac{\mathrm{D}v}{\mathrm{D}t}\right)\bigg|_z^h + 2\Omega_1 \int_z^h u_x \,\mathrm{d}s + 2\Omega_2 \int_z^h u_y \,\mathrm{d}s + 2\Omega_3 u\bigg|_z^h - 2\dot{\Omega}_1(h-z)$$
$$+ 2\Omega_1 V h_y + 2\Omega_1 \int_z^h v_y \,\mathrm{d}s - 2\Omega_2 U h_y - 2\Omega_2 \int_z^h u_y \,\mathrm{d}s$$
$$- \left(\Omega_1^2 + \Omega_2^2\right)(h+d_3)h_y - \beta_y(h-z) - \beta h_y - \sigma \partial_y \mathrm{div}(\boldsymbol{\kappa}), \tag{A 7}$$

or

$$\frac{\mathrm{D}v}{\mathrm{D}t} + \frac{1}{\rho}\frac{\partial p}{\partial y} = \frac{\mathrm{D}v}{\mathrm{D}t}\bigg|^h + \frac{\mathrm{D}w}{\mathrm{D}t}\bigg|^h h_y - 2\Omega_1 W + 2\Omega_3 U - 2\dot{\Omega}_1(h-z)$$
$$+ 2\Omega_1 V h_y - 2\Omega_2 U h_y + 2\Omega_1 w - 2\Omega_3 u$$
$$- \left(\Omega_1^2 + \Omega_2^2\right)(h+d_3)h_y - \beta_y(h-z) - \beta h_y - \sigma \partial_y \mathrm{div}(\boldsymbol{\kappa}), \tag{A 8}$$

which is (3.6) in § 3.

Appendix B. Verification of potential vorticity conservation

In this appendix, the conservation of the generalization of PV stated in (8.3) is proved. It is clear that the projection of the angular velocity onto the normal vector is important; so define

$$f(x, y, t) := \Omega_3 - \Omega_1 h_x - \Omega_2 h_y = \ell\, \boldsymbol{n} \cdot \boldsymbol{\Omega}, \tag{B 1}$$

and re-write the surface SWEs emphasizing the role of f,

$$\left.\begin{aligned} U_t + UU_x + VU_y + ah_x - 2fV &= \widehat{b}_1, \\ V_t + UV_x + VV_y + ah_y + 2fU &= \widehat{b}_2, \end{aligned}\right\} \tag{B 2}$$

where $a = a_{11} - 2\Omega_1 V$, $\widehat{b}_1 = b_1 - 2\Omega_3 V$, $\widehat{b}_2 = b_2 + 2\Omega_3 U$ and a_{11}, b_1 and b_2 are given in (4.6), (4.8) and (4.12), respectively. In the vorticity equation, only the derivatives of a, $\widehat{b}_1$ and $\widehat{b}_2$ appear, and they are

$$\left.\begin{aligned} a_x &= -\left(\Omega_1^2 + \Omega_2^2\right)h_x - \dot{\Omega}_2 + \Omega_1\Omega_3, \quad a_y = -\left(\Omega_1^2 + \Omega_2^2\right)h_y + \dot{\Omega}_1 + \Omega_2\Omega_3, \\ (\widehat{b}_1)_y &= -2\Omega_2 h_{yt} + \dot{\Omega}_3 - \Omega_1\Omega_2 - (\dot{\Omega}_2 + \Omega_1\Omega_3)h_y, \\ (\widehat{b}_2)_x &= 2\Omega_1 h_{xt} - \dot{\Omega}_3 - \Omega_1\Omega_2 + (\dot{\Omega}_1 - \Omega_2\Omega_3)h_x. \end{aligned}\right\} \tag{B 3}$$

Differentiate the second equation of (B 2) with respect to x and the first with respect to y:

$$\frac{\mathrm{D}(V_x - U_y)}{\mathrm{D}t} + (V_x - U_y)(U_x + V_y) + a_x h_y - a_y h_x + 2(fU)_x + 2(fV)_y = \frac{\partial \widehat{b}_2}{\partial x} - \frac{\partial \widehat{b}_1}{\partial y}. \tag{B 4}$$

Then substituting (B 3) gives

$$\frac{\mathrm{D}}{\mathrm{D}t}(V_x - U_y + 2f) + (V_x - U_y + 2f)(U_x + V_y) = 0. \tag{B 5}$$

Noting that $V_x - U_y + 2f = h$ PV, and using the mass equation, $(\mathrm{D}h/\mathrm{D}t) + h(U_x + V_y) = 0$, confirms that

$$\frac{\mathrm{D}}{\mathrm{D}t}(\mathrm{PV}) = 0. \tag{B 6}$$

Appendix C. Parameterizing rotations using Euler angles

Euler angles are the most widely used parameterization of rotations, and can be found in almost every textbook on analytical dynamics, ship dynamics and spacecraft dynamics. It is straightforward to write down an Euler-angle representation. The key issue with Euler angles is getting the angular velocity right, and making the correct distinction between the body representation and the space representation. For the purposes of this paper, we have found the treatment in O'Reilly (2008) the most complete. In this appendix, we record the representations of $\boldsymbol{Q}$ and the body representation of the angular velocity used in the paper.

Roll–pitch motion is the simplest non-commutative rotation that is of interest in ship dynamics. The roll–pitch excitation has been used by a number of authors for forced sloshing (e.g. Pantazopoulos 1987, 1988; Huang 1995; Huang & Hsiung 1996, 1997; Faltinsen *et al.* 2006*b*).

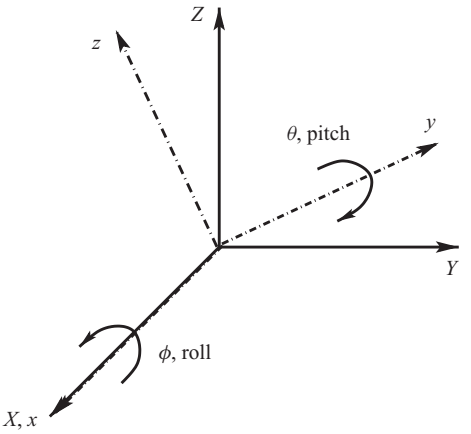

FIGURE 17. Schematic of the roll–pitch motion in terms of Euler angles ϕ and θ.

First, the properties of the Euler-angle representation of roll–pitch are recorded. The roll–pitch rotation consists of a counterclockwise roll rotation about the x-axis with angle ϕ, followed by a counterclockwise pitch rotation about the current y-axis, as schematically illustrated in figure 17. After converting both rotations to the same basis, the rotation matrix takes the form

$$\boldsymbol{Q} = \begin{bmatrix} \cos\theta & 0 & \sin\theta \\ \sin\phi\sin\theta & \cos\phi & -\sin\phi\cos\theta \\ -\cos\phi\sin\theta & \sin\phi & \cos\phi\cos\theta \end{bmatrix}. \tag{C 1}$$

From this expression, the body representation of the angular velocity is easily deduced using $\boldsymbol{Q}^{\mathrm{T}}\dot{\boldsymbol{Q}} = \widehat{\boldsymbol{\Omega}}$ and so

$$\boldsymbol{\Omega} = \begin{pmatrix} \dot{\phi}\cos\theta \\ \dot{\theta} \\ \dot{\phi}\sin\theta \end{pmatrix}. \tag{C 2}$$

The spatial angular velocity is obtained by multiplication of $\boldsymbol{\Omega}$ by $\boldsymbol{Q}$. A derivation of the roll–pitch angular velocity from first principles is given in Alemi Ardakani & Bridges (2009*c*).

If θ and ϕ are considered to be small, then the approximate body angular velocity is

$$\boldsymbol{\Omega} \approx \left(\dot{\phi}, \dot{\theta}, 0\right), \tag{C 3}$$

obtained by neglecting quadratic and higher order terms in (C 2). This simplified version of the angular velocity has been used by Pantazopoulos (1987, 1988), Falzarano *et al.* (2002) and Faltinsen *et al.* (2006*b*). However, this simplification makes the body and spatial representations of the angular velocity equal and so it destroys a key qualitative property of the rotation (cf. discussion in § 9.1).

C.1. *Yaw–pitch–roll rotation and 3–2–1 Euler angles*

The yaw–pitch–roll rotation is one of the most widely used Euler-angle sequences. (See § 6.8.1 of O'Reilly (2008), where they are called the 3–2–1 Euler-angle sequence.) It was first used in the context of sloshing by Huang (1995) and Huang & Hsiung (1996, 1997).

The 3–2–1 Euler-angle sequence starts with a yaw rotation about the z-axis with angle ψ, followed by a pitch rotation about the new y-axis denoted by θ, followed by a roll rotation about the new x-axis denoted by ϕ. The composite rotation is

$$\boldsymbol{Q} = \begin{bmatrix} \cos\theta\cos\psi & \sin\phi\sin\theta\cos\psi - \cos\phi\sin\psi & \cos\phi\sin\theta\cos\psi + \sin\phi\sin\psi \\ \cos\theta\sin\psi & \sin\phi\sin\theta\sin\psi + \cos\phi\cos\psi & \cos\phi\sin\theta\sin\psi - \sin\phi\cos\psi \\ -\sin\theta & \sin\phi\cos\theta & \cos\phi\cos\theta \end{bmatrix}. \tag{C 4}$$

The body angular velocity is computed to be

$$\boldsymbol{\Omega} = \begin{pmatrix} \dot{\phi} - \dot{\psi}\sin\theta \\ \dot{\psi}\cos\theta\sin\phi + \dot{\theta}\cos\phi \\ \dot{\psi}\cos\theta\cos\phi - \dot{\theta}\sin\phi \end{pmatrix}. \tag{C 5}$$

Full details of the 3–2–1 Euler angles and the derivation of the angular velocity are given in Alemi Ardakani & Bridges (2009*b*).

In matrix form, the angular velocity is related to the Euler angles by

$$\boldsymbol{\Omega} = \boldsymbol{B}^{-1}\dot{\Theta}, \tag{C 6}$$

with

$$\boldsymbol{B} = \begin{bmatrix} 1 & \sin\phi\tan\theta & \cos\phi\tan\theta \\ 0 & \cos\phi & -\sin\phi \\ 0 & \sin\phi\sec\theta & \cos\phi\sec\theta \end{bmatrix} \quad \text{and} \quad \Theta := \begin{pmatrix} \phi \\ \theta \\ \psi \end{pmatrix}. \tag{C 7}$$

This is the form of the angular velocity used in Huang (1995) and Huang & Hsiung (1997). The singularity of this Euler-angle representation arises due to the non-invertibility of $\boldsymbol{B}$:

$$\det(\boldsymbol{B}) = \sec\theta, \tag{C 8}$$

and so to avoid the singularity, the restriction $-(1/2)\pi < \theta < (1/2)\pi$ is required. For some applications, e.g. sloshing in a moving ship, this restriction is not severe, but for others, e.g. space applications, it is a restriction. If all three angles are small, then $\boldsymbol{B}$ is approximately the identity and $\boldsymbol{\Omega} \approx (\dot{\phi}, \dot{\theta}, \dot{\psi})$. The pitfalls of this approximation are discussed in § 9.1.

Appendix D. Details of the discretization

In this appendix, a sketch of the numerical discretization is given. Complete details can be found in Alemi Ardakani & Bridges (2009*e*).

Rewrite the governing equations (4.5)–(4.9), with the assumptions (7.3) and (7.4) in a form suitable for the first half-step of the scheme,

$$\left.\begin{aligned} &h_t + h^\star U_x + U^\star h_x + hV_y + Vh_y = 0, \\ &U_t + U^\star U_x + VU_y + 2\Omega_2 Vh_y + 2\Omega_2 h_t + \left[\alpha(x,y,t) + 2\Omega_1 V^\star \right. \\ &\quad \left. - \left(\Omega_1^2 + \Omega_2^2\right) h^\star\right] h_x = 2\Omega_3 V - (\dot{\Omega}_2 + \Omega_1\Omega_3)h + \widehat{\beta}(x,y,t), \\ &V_t + U^\star V_x + VV_y - 2\Omega_1 U^\star h_x - 2\Omega_1 h_t + \left[\alpha(x,y,t) - 2\Omega_2 U \right. \\ &\quad \left. - \left(\Omega_1^2 + \Omega_2^2\right) h\right] h_y = -2\Omega_3 U + (\dot{\Omega}_1 - \Omega_2\Omega_3)h + \widetilde{\beta}(x,y,t), \end{aligned}\right\} \tag{D 1}$$

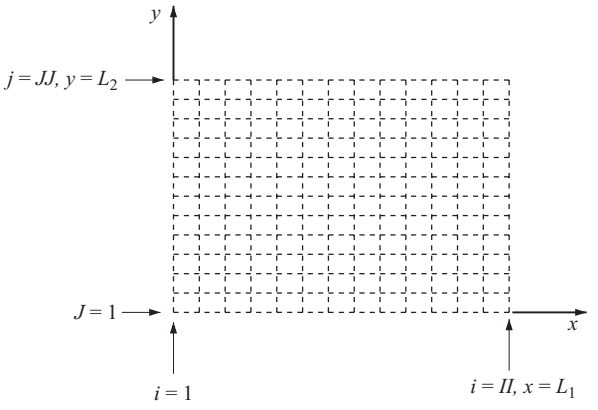

FIGURE 18. A schematic of the grid layout.

where α, $\widehat{\beta}$ and $\widetilde{\beta}$ are the terms that are independent of h, U and V,

$$\left.\begin{aligned}
\alpha(x,y,t) &= -\left(\Omega_1^2+\Omega_2^2\right)d_3+\left(\dot{\Omega}_1+\Omega_2\Omega_3\right)(y+d_2)\\
&\quad+\left(\Omega_1\Omega_3-\dot{\Omega}_2\right)(x+d_1)+\boldsymbol{Qe}_3\cdot\ddot{\boldsymbol{q}}+g\boldsymbol{Qe}_3\cdot\boldsymbol{e}_3,\\
\widehat{\beta}(x,y,t) &= -\left(\dot{\Omega}_2+\Omega_1\Omega_3\right)d_3+\left(\dot{\Omega}_3-\Omega_1\Omega_2\right)(y+d_2)\\
&\quad+\left(\Omega_2^2+\Omega_3^2\right)(x+d_1)-\boldsymbol{Qe}_1\cdot\ddot{\boldsymbol{q}}-g\boldsymbol{Qe}_1\cdot\boldsymbol{e}_3,\\
\widetilde{\beta}(x,y,t) &= \left(\dot{\Omega}_1-\Omega_2\Omega_3\right)d_3-\left(\dot{\Omega}_3+\Omega_1\Omega_2\right)(x+d_1)\\
&\quad+\left(\Omega_1^2+\Omega_3^2\right)(y+d_2)-\boldsymbol{Qe}_2\cdot\ddot{\boldsymbol{q}}-g\boldsymbol{Qe}_2\cdot\boldsymbol{e}_3.
\end{aligned}\right\}\tag{D 2}$$

The terms with $\star$ superscript are nonlinear terms that are treated implicitly. In this first half-step, only x-derivatives are implicit and y-derivatives are explicit. The nonlinearity is addressed using iteration.

The x-interval $0\leqslant x\leqslant L_1$ is split into $II-1$ intervals of length $\Delta x=L_1/(II-1)$ and so

$$x_i := (i-1)\Delta x,\quad i=1,\ldots,II,\tag{D 3}$$

and the y-interval, $0\leqslant y\leqslant L_2$, is split into $JJ-1$ intervals of length $\Delta y=L_2/(JJ-1)$ and so

$$y_j := (j-1)\Delta y,\quad j=1,\ldots,JJ,\tag{D 4}$$

and

$$h^n_{i,j} := h(x_i,y_j,t_n),\quad U^n_{i,j} := U(x_i,y_j,t_n)\quad\text{and}\quad V^n_{i,j} := V(x_i,y_j,t_n),\tag{D 5}$$

where $t_n=n\Delta t$, with Δt being the fixed time step. A schematic of the grid is shown in figure 18.

The discretization of the mass equation is

$$\begin{aligned}
&\frac{h^{n+(1/2)}_{i,j}-h^n_{i,j}}{(1/2)\Delta t}+h^\star_{i,j}\frac{U^{n+(1/2)}_{i+1,j}-U^{n+(1/2)}_{i-1,j}}{2\Delta x}+U^\star_{i,j}\frac{h^{n+(1/2)}_{i+1,j}-h^{n+(1/2)}_{i-1,j}}{2\Delta x}\\
&\qquad+h^n_{i,j}\frac{V^n_{i,j+1}-V^n_{i,j-1}}{2\Delta y}+V^n_{i,j}\frac{h^n_{i,j+1}-h^n_{i,j-1}}{2\Delta y}=0.
\end{aligned}\tag{D 6}$$

The discretizations of the equations for U, V are

$$\left.\begin{aligned}
&\frac{U_{i,j}^{n+(1/2)}-U_{i,j}^{n}}{(1/2)\Delta t}+U_{i,j}^{\star}\frac{U_{i+1,j}^{n+(1/2)}-U_{i-1,j}^{n+(1/2)}}{2\Delta x}+V_{i,j}^{n}\frac{U_{i,j+1}^{n}-U_{i,j-1}^{n}}{2\Delta y}+2\Omega_2^{n+(1/2)}V_{i,j}^{n}\\
&\times\frac{h_{i,j+1}^{n}-h_{i,j-1}^{n}}{2\Delta y}+\left[\alpha_{i,j}^{n+(1/2)}+2\Omega_1^{n+(1/2)}V_{i,j}^{\star}-\left(\left(\Omega_1^{n+(1/2)}\right)^2+\left(\Omega_2^{n+(1/2)}\right)^2\right)h_{i,j}^{\star}\right]\\
&\times\frac{h_{i+1,j}^{n+(1/2)}-h_{i-1,j}^{n+(1/2)}}{2\Delta x}=2\Omega_3^{n+(1/2)}V_{i,j}^{n+(1/2)}-\left(\dot{\Omega}_2^{n+(1/2)}+\Omega_1^{n+(1/2)}\Omega_3^{n+(1/2)}\right)h_{i,j}^{n+(1/2)}\\
&-2\Omega_2^{n+(1/2)}\frac{h_{i,j}^{n+(1/2)}-h_{i,j}^{n}}{(1/2)\Delta t}+\widehat{\beta}_{i,j}^{n+(1/2)},\\
&\frac{V_{i,j}^{n+(1/2)}-V_{i,j}^{n}}{(1/2)\Delta t}+U_{i,j}^{\star}\frac{V_{i+1,j}^{n+(1/2)}-V_{i-1,j}^{n+(1/2)}}{2\Delta x}+V_{i,j}^{n}\frac{V_{i,j+1}^{n}-V_{i,j-1}^{n}}{2\Delta y}-2\Omega_1^{n+(1/2)}U_{i,j}^{\star}\\
&\times\frac{h_{i+1,j}^{n+(1/2)}-h_{i-1,j}^{n+(1/2)}}{2\Delta x}+\left[\alpha_{i,j}^{n+(1/2)}-2\Omega_2^{n+(1/2)}U_{i,j}^{n}-\left(\left(\Omega_1^{n+(1/2)}\right)^2+\left(\Omega_2^{n+(1/2)}\right)^2\right)h_{i,j}^{n}\right]\\
&\times\frac{h_{i,j+1}^{n}-h_{i,j-1}^{n}}{2\Delta y}=-2\Omega_3^{n+(1/2)}U_{i,j}^{n+(1/2)}+\left(\dot{\Omega}_1^{n+(1/2)}-\Omega_2^{n+(1/2)}\Omega_3^{n+(1/2)}\right)h_{i,j}^{n+(1/2)}\\
&+2\Omega_1^{n+(1/2)}\frac{h_{i,j}^{n+(1/2)}-h_{i,j}^{n}}{(1/2)\Delta t}+\widetilde{\beta}_{i,j}^{n+(1/2)},
\end{aligned}\right\}\tag{D 7}$$

where

$$\alpha_{i,j}^{n}:=\alpha(x_i,y_j,t_n),\quad \widehat{\beta}_{i,j}^{n}:=\widehat{\beta}(x_i,y_j,t_n)\quad\text{and}\quad \widetilde{\beta}_{i,j}^{n}:=\widetilde{\beta}(x_i,y_j,t_n).\tag{D 8}$$

By setting

$$\boldsymbol{z}_{i,j}^{n}=\begin{bmatrix}h_{i,j}^{n}\\U_{i,j}^{n}\\V_{i,j}^{n}\end{bmatrix},$$

(D 6)–(D 7) can be written in block tridiagonal form as follows:

$$\begin{aligned}
&-{}_{\star}\boldsymbol{A}_{i,j}^{n+(1/2)}\boldsymbol{z}_{i-1,j}^{n+(1/2)}+\boldsymbol{B}^{n+(1/2)}\boldsymbol{z}_{i,j}^{n+(1/2)}+{}_{\star}\boldsymbol{A}_{i,j}^{n+(1/2)}\boldsymbol{z}_{i+1,j}^{n+(1/2)}\\
&\quad=\boldsymbol{C}_{i,j}^{n+(1/2)}\boldsymbol{z}_{i,j-1}^{n}+\boldsymbol{D}^{n+(1/2)}\boldsymbol{z}_{i,j}^{n}-\boldsymbol{C}_{i,j}^{n+(1/2)}\boldsymbol{z}_{i,j+1}^{n}+\boldsymbol{\beta}_{i,j}^{n+(1/2)}.
\end{aligned}\tag{D 9}$$

The left subscript $\star$ is an indication that the matrix depends on $h^{\star}$ and/or $U^{\star}$. Expressions for the matrices are given in Alemi Ardakani & Bridges (2009*e*). For fixed $j=2,\ldots,JJ-1$, (D 9) are applied for $i=2,\ldots,II-1$. To complete the tridiagonal system, equations are needed (for each fixed j) at $i=1$ and $i=II$.

D.1. *The equations at $i=1$ and $i=II$ for $j=2,\ldots,JJ-1$*

The purpose of this subsection is to show how the boundary conditions can be implemented exactly, even at the half-step.

The equations at $i=1$ and $i=II$ are obtained from the boundary conditions at $x=0$ and $x=L_1$. The only boundary condition at $x=0$ is $U(0,y,t)=0$. The discrete version of this is

$$U_{1,j}^{n}=0\quad\text{and}\quad\frac{U_{0,j}^{n}+U_{2,j}^{n}}{2}=0,\quad\text{for each } j,\quad\text{and for all}\quad n\in\mathbb{N}.\tag{D 10}$$

To obtain a boundary condition for h, use the mass equation at $x=0$

$$h_t + h^\star U_x + hV_y + Vh_y = 0, \tag{D 11}$$

with discretization

$$h_{1,j}^{n+(1/2)} + \frac{\Delta t}{2\Delta x} h_{1,j}^\star U_{2,j}^{n+(1/2)} = h_{1,j}^n - \frac{\Delta t}{4\Delta y} h_{1,j}^n \left(V_{1,j+1}^n - V_{1,j-1}^n\right) - \frac{\Delta t}{4\Delta y} V_{1,j}^n \left(h_{1,j+1}^n - h_{1,j-1}^n\right). \tag{D 12}$$

To obtain a boundary condition for V, use the y-momentum equation at $x=0$,

$$V_t + VV_y - 2\Omega_1 h_t + \left[\alpha(x,y,t) - \left(\Omega_1^2 + \Omega_2^2\right) h\right] h_y = (\dot{\Omega}_1 - \Omega_2\Omega_3)h + \widetilde{\beta}(x,y,t), \tag{D 13}$$

with discretization

$$\begin{aligned} V_{1,j}^{n+(1/2)} - \left[2\Omega_1^{n+(1/2)} + (1/2)\Delta t\left(\dot{\Omega}_1^{n+(1/2)} - \Omega_2^{n+(1/2)}\Omega_3^{n+(1/2)}\right)\right] h_{1,j}^{n+(1/2)} \\ = V_{1,j}^n - \frac{\Delta t}{4\Delta y} V_{1,j}^n \left(V_{1,j+1}^n - V_{1,j-1}^n\right) - \frac{\Delta t}{4\Delta y} \widehat{\alpha_{1,j}^{n+(1/2)}} \left(h_{1,j+1}^n - h_{1,j-1}^n\right) \\ - 2\Omega_1^{n+(1/2)} h_{1,j}^n + (1/2)\Delta t \widetilde{\beta}_{1,j}^{n+\frac{1}{2}}, \end{aligned} \tag{D 14}$$

where

$$\widehat{\alpha_{i,j}^n} = \alpha_{i,j}^n - \left(\left(\Omega_1^n\right)^2 + \left(\Omega_2^n\right)^2\right) h_{i,j}^{n-(1/2)}. \tag{D 15}$$

Combining (D 10), (D 12) and (D 14) gives the following equation for $i=1$:

$$\boldsymbol{E}^{n+(1/2)} \boldsymbol{z}_{1,j}^{n+(1/2)} + {}_\star\boldsymbol{F}_{1,j} \boldsymbol{z}_{2,j}^{n+(1/2)} = \boldsymbol{G}_{1,j}^{n+(1/2)} \boldsymbol{z}_{1,j-1}^n + \boldsymbol{H}^{n+(1/2)} \boldsymbol{z}_{1,j}^n - \boldsymbol{G}_{1,j}^{n+(1/2)} \boldsymbol{z}_{1,j+1}^n + {}_1\boldsymbol{\beta}_{1,j}^{n+(1/2)}. \tag{D 16}$$

Expressions for the matrices are given in Alemi Ardakani & Bridges (2009*e*). A similar strategy is used to construct the discrete equations at $x=L_1$.

D.2. *Summary of the equations for* $j=2,\ldots,JJ-1$

This completes the construction of the block tridiagonal system at j-interior points. For each fixed $j=2,\ldots,JJ-1$, and fixed $h^\star$, $U^\star$ and $V^\star$, we solve the following block tridiagonal system:

$$\left.\begin{aligned} \boldsymbol{E}^{n+(1/2)} \boldsymbol{z}_{1,j}^{n+(1/2)} + {}_\star\boldsymbol{F}_{1,j} \boldsymbol{z}_{2,j}^{n+(1/2)} &= \boldsymbol{G}_{1,j}^{n+(1/2)} \boldsymbol{z}_{1,j-1}^n + \boldsymbol{H}^{n+(1/2)} \boldsymbol{z}_{1,j}^n - \boldsymbol{G}_{1,j}^{n+(1/2)} \boldsymbol{z}_{1,j+1}^n + {}_1\boldsymbol{\beta}_{1,j}^{n+(1/2)}, \\ -{}_\star\boldsymbol{A}_{2,j}^{n+(1/2)} \boldsymbol{z}_{1,j}^{n+(1/2)} + \boldsymbol{B}^{n+(1/2)} \boldsymbol{z}_{2,j}^{n+(1/2)} + {}_\star\boldsymbol{A}_{2,j}^{n+(1/2)} \boldsymbol{z}_{3,j}^{n+(1/2)} &= \boldsymbol{C}_{2,j}^{n+(1/2)} \boldsymbol{z}_{2,j-1}^n + \boldsymbol{D}^{n+(1/2)} \boldsymbol{z}_{2,j}^n - \boldsymbol{C}_{2,j}^{n+(1/2)} \boldsymbol{z}_{2,j+1}^n + \boldsymbol{\beta}_{2,j}^{n+(1/2)}, \\ -{}_\star\boldsymbol{A}_{3,j}^{n+(1/2)} \boldsymbol{z}_{2,j}^{n+(1/2)} + \boldsymbol{B}^{n+(1/2)} \boldsymbol{z}_{3,j}^{n+(1/2)} + {}_\star\boldsymbol{A}_{3,j}^{n+(1/2)} \boldsymbol{z}_{4,j}^{n+(1/2)} &= \boldsymbol{C}_{3,j}^{n+(1/2)} \boldsymbol{z}_{3,j-1}^n + \boldsymbol{D}^{n+(1/2)} \boldsymbol{z}_{3,j}^n - \boldsymbol{C}_{3,j}^{n+(1/2)} \boldsymbol{z}_{3,j+1}^n + \boldsymbol{\beta}_{3,j}^{n+(1/2)}, \\ &\vdots \quad \vdots \\ -{}_\star\boldsymbol{F}_{II,j} \boldsymbol{z}_{II-1,j}^{n+(1/2)} + \boldsymbol{E}^{n+(1/2)} \boldsymbol{z}_{II,j}^{n+(1/2)} &= \boldsymbol{G}_{II,j}^{n+(1/2)} \boldsymbol{z}_{II,j-1}^n + \boldsymbol{H}^{n+(1/2)} \boldsymbol{z}_{II,j}^n - \boldsymbol{G}_{II,j}^{n+(1/2)} \boldsymbol{z}_{II,j+1}^n + {}_1\boldsymbol{\beta}_{II,j}^{n+(1/2)}. \end{aligned}\right\} \tag{D 17}$$

Special boundary systems are constructed for the lines $j = 1$ and $j = JJ$. These systems are constructed exactly using boundary conditions and the details are given in Alemi Ardakani & Bridges (2009*e*).

This completes the algorithm details for the first half-step, $n \mapsto n + (1/2)$. For each fixed $h^\star$ and $U^\star$, it involves solving a sequence of linear block tridiagonal system for each $j = 1, \ldots, JJ$. Then the process is repeated with updates of $h^\star$ and $U^\star$ till convergence, $h^\star \to h^{n+(1/2)}$ and $U^\star \to U^{n+(1/2)}$.

The second half-step is constructed similarly with x-derivatives explicit and y-derivatives implicit, and the integration is along vertical grid lines. The details are given in the report of Alemi Ardakani & Bridges (2009*e*).

Electronic versions of the technical reports, preprints and videos listed can be found at http://personal.maths.surrey.ac.uk/st/T.Bridges/SLOSH/.

REFERENCES

Abbott, M. B. 1979 *Computational Hydraulics: Elements of the Theory of Free-Surface Flows*. Pitman Publishers.

Adee, B. H. & Caglayan, I. 1982 The effects of free water on deck on the motions and stability of vessels. In *Proceedings of the Second International Conference Stab. Ships and Ocean Vehicles*, *Tokyo, Japan*, vol. 218, pp. 413–426. Springer.

Alemi Ardakani, H. & Bridges, T. J. 2009*a* Dynamic coupling between shallow-water sloshing and a vehicle undergoing planar rigid- body motion. *Tech. Rep.* Department of Mathematics, University of Surrey.

Alemi Ardakani, H. & Bridges, T. J. 2009*b* Review of the 3–2–1 Euler angles: a yaw–pitch–roll sequence. *Tech. Rep.* Department of Mathematics, University of Surrey.

Alemi Ardakani, H. & Bridges, T. J. 2009*c* Review of the Dillingham, Falzarano & Pantazopoulos three-dimensional shallow-water equations. *Tech. Rep.* Department of Mathematics, University of Surrey.

Alemi Ardakani, H. & Bridges, T. J. 2009*d* Review of the Huang–Hsiung three-dimensional shallow-water equations. *Tech. Rep.* Department of Mathematics, University of Surrey.

Alemi Ardakani, H. & Bridges, T. J. 2009*e* Shallow water sloshing in rotating vessels: details of the numerical algorithm. *Tech. Rep.* Department of Mathematics, University of Surrey.

Alemi Ardakani, H. & Bridges, T. J. 2009*f* Surge–sway simulations with additional detail. *Tech. Rep.* Department of Mathematics, University of Surrey.

Alemi Ardakani, H. & Bridges, T. J. 2010 Dynamic coupling between shallow water sloshing and horizontal vehicle motion. *Eur. J. Appl. Math.,* doi:10.1017/S0956792510000197.

Barnes, R. T. H., Hide, R., White, A. A. & Wilson, C. A. 1983 Atmospheric angular momentum fluctuations, length-of-day changes and polar motion. *Proc. R. Soc. Lond.* A **387**, 31–73.

Billingham, J. 2002 Nonlinear sloshing in zero gravity. *J. Fluid Mech.* **464**, 365–391.

Bridges, T. J. 1987 Secondary bifurcation and change of type for three-dimensional standing waves in finite depth. *J. Fluid Mech.* **179**, 137–153.

Bridges, T. J. 2009 Wave breaking and the surface velocity field for three-dimensional water waves. *Nonlinearity* **22**, 947–953.

Buchner, B. 2002 Green water on ship-type offshore structures. PhD thesis, Technical University of Delft.

Caglayan, I. & Storch, R. L. 1982 Stability of fishing vessels with water on deck: a review. *J. Ship Res.* **26**, 106–116.

Cariou, A. & Casella, G. 1999 Liquid sloshing in ship tanks: a comparative study of numerical simulation. *Marine Struct.* **12**, 183–198.

Chen, Y. G., Djidjeli, K. & Price, W. G. 2009 Numerical simulation of liquid sloshing phenomena in partially filled containers. *Comput. Fluids* **38**, 830–842.

Chen, Y.-H., Hwang, W.-S. & Ko, C.-H. 2000 Numerical simulation of the three-dimensional sloshing problem by boundary element method. *J. Chinese Inst. Engng* **23**, 321–330.

Dillingham, J. T. & Falzarano, J. M. 1986 Three-dimensional numerical simulation of green water on deck. In *3rd International Conference on Stability of Ships and Ocean Vehicles, Gdansk, Poland*, (ed. L. Kobylinski). Tech. U. Gdansk.

Dingemans, M. W. 1997 *Water Wave Propagation Over Uneven Bottoms. Part 2: Nonlinear Wave Propagation*. World Scientific.

Disimile, P. J., Pyles, J. M. & Toy, N. 2009 Hydraulic jump formation in water sloshing within an oscillating tank. *J. Aircraft* **46**, 549–556.

Evans, D. J. 1977 On the representation of orientation space. *Mol. Phys.* **34**, 317–325.

Faltinsen, O. M., Rognebakke, O. F. & Timokha, A. N. 2003 Resonant three-dimensional nonlinear sloshing in a square basin. *J. Fluid Mech.* **487**, 1–42.

Faltinsen, O. M., Rognebakke, O. F. & Timokha, A. N. 2006*a* Resonant three-dimensional nonlinear sloshing in a square-base basin. Part 3. Base ratio perturbations. *J. Fluid Mech.* **551**, 359–397.

Faltinsen, O. M., Rognebakke, O. F. & Timokha, A. N. 2006*b* Transient and steady-state amplitudes of resonant three-dimensional sloshing in a square base tank with finite fluid depth. *Phys. Fluids* **18**, 012103.

Faltinsen, O. M. & Timokha, A. N. 2003 An adaptive multimodal approach to nonlinear sloshing in a rectangular tank. *J. Fluid Mech.* **432**, 167–200.

Faltinsen, O. M. & Timokha, A. N. 2009 *Sloshing*. Cambridge University Press.

Gerrits, J. 2001 Dynamics of liquid-filled spacecraft. PhD thesis, University of Groningen, The Netherlands.

Hanson, A. J. 2006 *Visualizing Quaternions*. Morgan-Kaufmann/Elsevier.

Huang, Z. 1995 Nonlinear shallow water flow on deck and its effect on ship motion. PhD thesis, Technical University of Nova Scotia, Halifax, Canada.

Huang, Z. J. & Hsiung, C. C. 1996 Nonlinear shallow water on deck. *J. Ship Res.* **40**, 303–315.

Huang, Z. J. & Hsiung, C. C. 1997 Nonlinear shallow-water flow on deck coupled with ship motion. In *21st Symposium on Naval Hydrodynamics*, pp. 220–234. National Academies Press.

Ibrahim, R. A. 2005 *Liquid Sloshing Dynamics*. Cambridge University Press.

Kidambi, R. & Shankar, P. N. 2004 The effects of the contact angle on sloshing in containers. *Proc. R. Soc. Lond.* A **460**, 2251–2267.

Kim, Y. 2001 Numerical simulation of sloshing flows with impact load. *Appl. Ocean Res.* **23**, 53–62.

Kleefsman, K. M. T., Erwin Loots, G., Veldman, A. E. P., Buchner, B., Bunnik, T. & Falkenberg, E. 2005 The numerical simulation of green water loading including vessel motions and the incoming field. In *Proceedings of the 24th International Conference on Offshore Mechanics and Arctic Engineering (OMAE'05)*, vol. OMAE2005-67448, pp. 981–992, ASME.

Kobine, J. J. 2008 Nonlinear resonant characteristics of shallow fluid layers. *Phil. Trans. R. Soc. Lond.* A **366**, 1131–1346.

Laranjinha, M., Falzarano, J. M. & Guedes Soares, C. 2002 Analysis of the dynamical behaviour of an offshore supply vessel with water on deck. In *Proceedings of 21st International Conference Offshore Mechanics and Arctic Engineering*, *Paper No. OMAE2002-OFT28177*, vol. 1, pp. 383–390. ASME.

La Rocca, M., Mele, P. & Armenio, V. 1997 Variational approach to the problem of sloshing in a moving container. *J. Theor. Appl. Fluid Mech.* **1**, 280–310.

La Rocca, M., Sciortino, G. & Boniforti, M. A. 2000 A fully nonlinear model for sloshing in a rotating container. *Fluid Dyn. Res.* **27**, 23–52.

Lee, S. J., Kim, M. H., Lee, D. H., Kim, J. W. & Kim, Y. H. 2007 The effects of LNG-tank sloshing on the global motions of LNG carriers. *Ocean Engng* **34**, 10–20.

Lee, S. K., Surendran, S. & Lee, G. 2005 Roll performance of a small fishing vessel with live fish tank. *Ocean Engng* **32**, 1873–1885.

Leendertse, J. 1967 Aspects of a computational model for long-period water wave propagation. *Tech. Rep.* RM-5294-PR. Rand Corporation.

Leimkuhler, B. & Reich, S. 2004 *Simulating Hamiltonian Dynamics*. Cambridge University Press.

Leubner, C. 1981 Correcting a widespread error concerning the angular velocity of a rotating rigid body. *Am. J. Phys.* **49**, 232–234.

Liu, D. & Lin, P. 2008 A numerical study of three-dimensional liquid sloshing in tanks. *J. Comput. Phys.* **227**, 3921–3939.

McIntyre, M. E. 2003 Potential vorticity. In *Encyclopedia of Atmospheric Sciences* (ed. J. R. Holton, J. A. Pyle & J. A. Curry), vol. 2. Academic/Elsevier.

Miles, J. & Henderson, D. 1990 Parametrically forced surface waves. *Annu. Rev. Fluid Mech.* **22**, 143–165.

Murray, R. M., Lin, Z. X. & Sastry, S. S. 1994 *A Mathematical Introduction to Robotic Manipulation*. CRC Press.

Ockendon, J. R. & Ockendon, H. 1973 Resonant surface waves. *J. Fluid Mech.* **59**, 397–413.

O'Reilly, O. M. 2008 *Intermediate Dynamics for Engineers: A Unified Treatment of Newton–Euler and Lagrangian Mechanics*. Cambridge University Press.

Pantazopoulos, M. S. 1987 Numerical solution of the general shallow water sloshing problem. PhD thesis, University of Washington, Seattle, WA.

Pantazopoulos, M. S. 1988 Three-dimensional sloshing of water on decks. *Marine Technol.* **25**, 253–261.

Pantazopoulos, M. S. & Adee, B. H. 1987 Three-dimensional shallow water waves in an oscillating tank. In *Proc. ASCE Speciality Conference on Coastal Hydrodynamics*, (ed. R. A. Dalrymple) pp. 399–412.

Penney, W. G. & Price, A. T. 1952 Part II. Finite periodic stationary gravity waves in a perfect fluid. *Phil. Trans. R. Soc. Lond.* A **244**, 254–284.

Peregrine, D. H. 1998 Surf-zone currents. *Theor. Comput. Fluid Dyn.* **10**, 295–309.

Peregrine, D. H. 1999 Large-scale vorticity generation by breakers in shallow and deep water. *Eur. J. Mech.* B/*Fluids* **18**, 403–408.

Pomeau, Y., Le Berre, M., Guyenne, P. & Grilli, S. 2008*a* Wave breaking and generic singularities of nonlinear hyperbolic equations. *Nonlinearity* **21**, T61–T79.

Pomeau, Y., Jamin, T., Le Bars, M., Le Gal, P. & Audoly, B. 2008*b* Law of spreading of the crest of a breaking wave. *Proc. R. Soc. Lond.* A **464**, 1851–1866.

Pratt, L. J. 1983 On internal flow over topography. Part 1. Semigeostrophic adjustment to an obstacle. *J. Fluid Mech.* **131**, 195–218.

Rapaport, D. C. 1985 Molecular dynamics simulations using quaternions. *J. Comput. Phys.* **60**, 306–314.

Rebouillat, S. & Liksonov, D. 2010 Fluid–structure interaction in partially filled liquid containers: a comparative review of numerical approaches. *Comput. Fluids* **39**, 739–746.

Romero, I. 2008 Formulation and performance of variational integrators for rotating bodies. *Comput. Mech.* **42**, 825–836.

Ruponen, P., Matusiak, J., Luukkonen, J. & Ilus, M. 2009 Experimental study on the behavior of a swimming pool onboard a large passenger ship. *Marine Technol.* **46**, 27–33.

Salmon, R. 1998 *Lectures on Geophysical Fluid Dynamics*. Oxford University Press.

Taylor, G. I. 1953 An experimental study of standing waves. *Proc. R. Soc. Lond.* A **218**, 44–59.

Titterton, D. H. & Weston, J. L. 2004 *Strapdown Inertial Navigation Technology*, 2nd edn. Institute of Electrical Engineers.

Vanyo, J. P. 1993 *Rotating Fluids in Engineering and Science*. Butterworth-Heineman.

Veldman, A. E. P., Gerrits, J., Luppes, R., Helder, J. A. & Vreeburg, J. P. B. 2007 The numerical simulation of liquid sloshing on board spacecraft. *J. Comput. Phys.* **224**, 82–99.

aus der Wiesche, S. 2003 Computational slosh dynamics: theory and industrial application. *Comput. Mech.* **30**, 374–387.

Wiggins, S. 1987 Chaos in the quasiperiodically forced Duffing oscillator. *Phys. Lett.* A **124**, 138–142.

Wu, C.-H. & Chen, B.-F. 2009 Sloshing waves and resonance modes of fluid in a 3D tank by a time-independent finite difference method. *Ocean Engng* **36**, 500–510.

Wu, G. S., Ma, Q. W. & Eatock Taylor, R. 1998 Numerical simulation of sloshing waves in a 3D tank based on a finite element method. *Appl. Ocean Res.* **20**, 337–355.

Zhou, Z., De Kat, J. O. & Buchner, B. 1999 A nonlinear 3D approach to simulate green water dynamics on deck. In *Proceedings of the 7th International Conference Numer. Ship Hydro.* (ed. J. Piquet), *Nantes, France*, vol. 7. DTIC.